Lyle, M., Wilson, P.A., Janecek, T.R., et al., 2002
Proceedings of the Ocean Drilling Program, Initial Reports Volume 199

15. SITE 1222[1]

Shipboard Scientific Party[2]

F1. Site location map, p. 18.

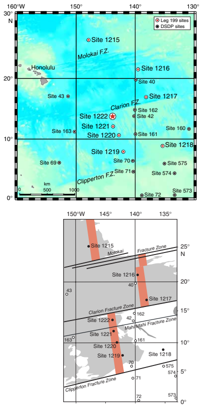

BACKGROUND AND OBJECTIVES

Site 1222 (13°48.98′N, 143°53.35′W; 4989 meters below sea level [mbsl]; Fig. **F1**) forms a south-central component of the 56-Ma transect drilled during Leg 199 and is situated ~2° south of the Clarion Fracture Zone in typical abyssal hill topography. On the basis of regional magnetic anomalies, we anticipated basement age at Site 1222 to be equivalent to Chron C25r or Chron C25n (~56–57 Ma) (Cande et al., 1989), which is slightly older than at Site 1219. At the outset of drilling at Site 1222, our estimate for total sediment thickness was ~115 m (Fig. **F2**).

F2. Seismic reflection profile, p. 19.

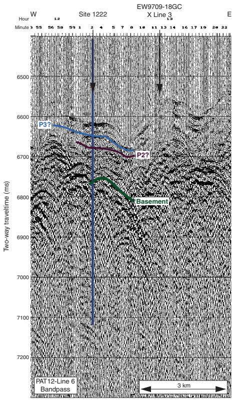

Based upon a fixed hotspot model (Gripp and Gordon, 1990, for 0- to 5-Ma Pacific hotspot rotation pole; Engebretson et al., 1985, for older poles) Site 1222 should have been located ~1° north of the equator at 56 Ma and ~4°N at 40 Ma. A nearby gravity core (EW9709-17GC), taken during the site survey cruise, recovered >5 m of red clay with a late–middle Miocene age on the basis of radiolarian biostratigraphy (Lyle, 2000). Deep Sea Drilling Project (DSDP) Site 42 located ~4° east of Site 1222, was not drilled to basement but contains a thin sedimentary section (~100 m thick) of upper Oligocene nannofossil ooze through middle Eocene radiolarian nannofossil ooze. In turn, DSDP Site 162 lies ~1° north of DSDP Site 42 and is situated on young crust (49 Ma) that contains ~150 m of clayey radiolarian and nannofossil oozes of early Oligocene–middle Eocene age.

Site 1222 will be used to study the position of the Intertropical Convergence Zone in the late Eocene and Oligocene, to sample late Paleocene and early Eocene sediments in the central tropical Pacific Ocean, and to help determine whether or not there has been significant southward movement of the hotspots with respect to the spin axis prior to 40 Ma.

---

[1] **Examples of how to reference the whole or part of this volume.**

[2] **Shipboard Scientific Party addresses.**

Ms 199IR-115

SUMMARY

Site 1222 (13°48.98′N, 143°53.35′W) is situated ~2° south of the Clarion Fracture Zone in typical abyssal hill topography at a water depth of 4989 m. On the basis of regional seafloor magnetic anomalies, we anticipated basement age at Site 1222 to be equivalent to Anomaly An25 (~56–57 Ma) (Cande et al., 1989), which is slightly older than at Site 1219. At the onset of drilling at Site 1222, our estimate for total sediment thickness was ~115 m, based upon a fixed hotspot model (Gripp and Gordon, 1990, for the 0- to 5-Ma Pacific hotspot rotation pole; Engebretson et al., 1985, for older poles). Site 1222 should have been located ~1° north of the equator at 56 Ma and ~4°N at 40 Ma.

Two holes were drilled at Site 1222. Hole 1222A was drilled to basement, which was reached at ~98 meters below seafloor (mbsf). Hole 1222B recored the advanced piston corer (APC)-suitable portion of the sediment column (to ~60 mbsf). The sediment column at Site 1222 contains a sequence of lithologies significantly different from that found at other Leg 199 sites. At Site 1222, we recovered a 97.8-m-thick section dominated by clay-rich lithologies and chert. Unit I consists of an ~55-m-thick yellowish brown to dark gray-brown clay with zeolites grading to radiolarian clay. A thin interval of diatomaceous clay is present near 17 mbsf (Sections 199-1222A-3H-2 to 3H-4). Within the diatom clay is an interval with unusual layers of laminated diatom ooze that contain a nearly pure diatom component of Pliocene age. Laminations are mainly white to olive. Diatom frustules within some laminae contain significant pyrite, which makes them appear very dark gray to black. A sharp contact exists at the base of the diatom ooze interval and the underlying clay of Subunit IA. In Hole 1222A, this contact also contains a large (5 cm diameter) botryoidal manganese nodule. Unit II, ~3 m thick, consists of dark brown to brown nannofossil clay grading downcore to yellowish brown nannofossil ooze. Very pale brown mottles are common. Nannofossil content (estimated from smear slides) gradually increases from 30% in the upper portion to 80% near the base of the unit. Unit III consists of an ~8-m-thick sequence dominated by clay with iron oxides and zeolites. Unit III is underlain by a thick (>30 m) poorly recovered sequence of massive chert that, in turn, overlies basement basalt.

Radiolarians provide the biostratigraphic framework for Site 1222. Planktonic foraminifers are completely dissolved in all samples investigated. Calcareous nannofossils of early Oligocene age are present in Unit II, and early Eocene nannofossils were found in chalk attached to a piece of chert that is present just above basement. This large chert nodule is rimmed with very pale brown nannofossil chalk that provides datums indicating an early Eocene age (NP10). The biostratigraphic distribution of radiolarians suggests massive reworking and mixed Pliocene assemblages in the uppermost two and a half cores (between ~0 and 21 mbsf). The following two cores (between ~21 and 40 mbsf) contain upper and lower Miocene radiolarian assemblages. Two cores between ~40 and 60 mbsf hold upper and lower Oligocene radiolarian assemblages. Nannofossils are present between ~55 and 60 mbsf, supporting the radiolarian biostratigraphy. This upper part of the section at Site 1222 appears to contain several breaks in sedimentation. A major hiatus is present between the lowermost Oligocene and the middle Eocene, having a duration on the order of ~5–6 m.y.

It was possible to construct a continuous spliced record from Site 1222 down to 34.44 mbsf (37.88 meters composite depth [mcd]), below

which it was possible to align most cores from the two drilled holes to each other but without continuous overlap. Cores 199-1222A-7H and 199-1222B-7H, however, showed good overlap and allowed the splicing of an additional ~13 m from ~59 to 72 mcd.

The paleomagnetic data from lithologic Subunit IA, down to (~40 mbsf) are not interpretable, except for the very top of Hole 1222A. A large group of characteristic remanent magnetization (ChRM) directions show relatively high magnetic inclinations after demagnetization especially in the most clay-rich lithologic units. The cause of the steep inclinations is unclear and might be indicative of unrecognized deformation and physical grain rotation caused by drilling. A preliminary correlation of the magnetic stratigraphy to the goemagnetic polarity timescale shows that at the very top of the section we were able to identify the bottom of polarity Chron C1n (Brunhes). Below 40 mcd, we note magnetic reversals but can only identify Chrons C6Cn to C11n with any confidence.

The pore water profiles from Site 1222 primarily reflect minor organic matter degradation and the dissolution of biogenic silica. Most of the dissolved chemical constituents show a lack of gradient with depth and values similar to or slightly higher than seawater.

OPERATIONS

Site 1222

Transit to Site 1222 (PAT-12C)

The 107-nmi voyage to proposed Site PAT-12C was accomplished in 10.5 hr at an average speed of 10.2 kt. The vessel proceeded directly to the site without conducting a survey. The Global Positioning System receiver interface to the dynamic positioning system was employed to situate the vessel over the coordinates of the new location by 0745 hr on 10 December 2001. A beacon was deployed at 0845 hr. The corrected precision depth recorder (PDR) depth was 5009.4 meters below rig floor (mbrf).

Hole 1222A

After the drill string was deployed to a depth of 4955 mbrf, the driller lowered the bit until the heave compensator appeared to activate, suggesting contact with a firm seafloor at ~5001 mbrf. The drill string was then picked up 5 m to position the bit at a depth of 4996 mbrf. Hole 1222A was spudded with the APC at 1815 hr on 10 December. The seafloor depth indicated by the recovery of the initial core was 5000.1 mbrf, 8.4 m shallower than the PDR depth.

Piston coring in Hole 1222A advanced to an APC refusal depth of 71.9 mbsf, with an average recovery of 102.9% (Table T1). Orientation began with Core 3H. The hole was further deepened with four extended core barrel (XCB) cores until basement contact at a depth of 107.3 mbsf. The average recovery for the 35.4-m XCB-cored section was 1.8%.

T1. Coring summary, p. 40.

Hole 1222B

After coring operations were completed in Hole 1222A, the drill pipe was pulled out of the hole, and after the bit cleared the seafloor at 1735 hr on 11 December, the vessel was offset 20 mi east of Hole 1222A. Hole

1222B was spudded with the APC at 1910 hr and coring advanced to refusal depth (64.4 mbsf) (Table **T1**). As Core 7H was brought on deck, the time allotted for coring expired. The average recovery for the hole was 99.0%. Orientation started with Core 3H.

After coring operations ceased in Hole 1222B, the drill string was recovered and the bottom-hole assembly was disassembled into component parts and was secured into the drill collar bays. During the recovery of the drill string, the beacon was successfully recalled. After the drilling equipment was secured, the drilling crew spent 1 hr cutting and slipping the drilling line. The vessel departed for Honolulu at 1730 hr on 12 December.

LITHOSTRATIGRAPHY

Site 1222 recovered a 97.8-m-thick section dominated by clay-rich lithologies and chert (Fig. **F3**). Fifty-five meters of lower Oligocene and younger clay with zeolites and radiolarian clay overlies 3.8 m of basal Oligocene nannofossil ooze. Eocene sediments are represented by clay and chert and are poorly recovered. The sedimentary section was divided into four units based on compositional differences. A fifth unit, seafloor basalt, was also recovered. Hole 1222A had better recovery and less core disturbance than Hole 1222B. For this reason, much of the following description is primarily based on sediments from Hole 1222A.

F3. Lithologic summary, p. 20.

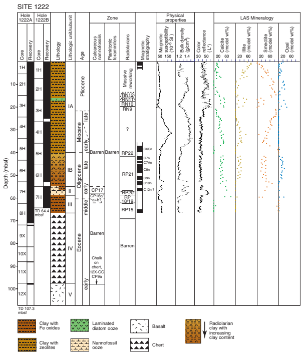

Unit I

Intervals: 199-1222A-1H, 0 cm, through 7H-2, 40 cm, and 199-1222B-1H, 0 cm, through 7H-5, 91 cm
Depths: 0–54.9 mbsf (Hole 1222A) and 0–61.8 mbsf (Hole 1222B)
Age: Holocene to early Oligocene
Lithology: Clay with zeolites grading to radiolarian clay

Unit I is divided into two subunits based upon lithologic components. A gradational contact exists between the subunits and with Unit II below.

Subunit IA

Intervals: 199-1222A-1H, 0 cm, through 5H-6, 10 cm, and 199-1222B-1H, 0 cm, through 6H-2, 40 cm
Depths: 0–40.5 mbsf (Hole 1222A) and 0–47.1 mbsf (Hole 1222B)
Age: Holocene to late Oligocene
Lithology: clay with zeolites

Subunit IA consists of light yellowish brown to very dark grayish brown (10YR 6/4 to 10YR 3/2) clay with zeolites. Zeolites (authigenic phillipsite) are common to abundant, especially in the lighter-colored (10YR 6/4) intervals. A minor amount of iron oxides and opaque minerals are also present, and a few small (2- to 3-mm diameter) manganese nodules are disseminated throughout this subunit. A thin interval of diatomaceous clay is present near 17 mbsf (intervals 199-1222A-3H-2, 21 cm, through 3H-4, 82 cm, and 199-1222B-2H-7, 35 cm, through 3H-2, 87 cm). Within the diatom ooze are several unusual layers of laminated diatom ooze that contain a nearly pure diatom component (Fig. **F4**). Laminations are mainly white to olive (5Y 8/1 to 5Y 5/3). Diatom frus-

F4. Laminated diatom ooze interval, p. 21.

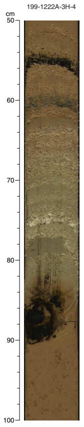

tules within some laminae contain significant amounts of pyrite, making them appear very dark gray to black (10YR 2/2 to 10YR 2/1). A sharp contact exists between the base of the diatom ooze interval and the underlying clay of Subunit IA. In Hole 1222A, this contact also contains a large (5 cm diameter) botryoidal manganese nodule (interval 199-1222A-3H-4, 80–85 cm).

Subunit IB

Intervals: 199-1222A-5H-6, 10 cm, through 7H-2, 40 cm, and 199-1222B-6H-2, 40 cm, through 7H-5, 91 cm
Depths: 40.5–54.9 mbsf (Hole 1222A) and 47.1–61.8 mbsf (Hole 1222B)
Age: late to early Oligocene
Lithology: radiolarian clay grading to clay with radiolarians

Subunit IB consists of very dark grayish brown to dark brown (10YR 3/2 to 10YR 3/3) radiolarian clay. Bioturbation is slight to moderate throughout this interval causing some yellowish brown to brown (10YR 5/6 to 10YR 5/3) mottling. Radiolarian content varies only slightly, comprising ~40% of the lithology. Minor components include oxide minerals, zeolites, volcanic glass, and sponge spicules.

Unit II

Intervals: 199-1222A-7H-2, 40 cm, through 7H-4, 130 cm, and 199-1222B-7H-5, 91 cm, through 7H-CC
Depths: 54.9–58.7 mbsf (Hole 1222A) and 61.8–64.4 mbsf base of hole (Hole 1222B)
Age: early Oligocene
Lithology: nannofossil ooze

This unit consists of dark brown to brown (10YR 3/3 to 10YR 4/3) nannofossil clay grading downcore to yellowish brown (10YR 5/4) nannofossil ooze. Very pale brown (10YR 8/2) mottles are common. Nannofossil content (estimated from smear slides) gradually increases from 30% in the upper portion to 80% near the base of the unit. Minor amounts of iron oxides, zeolites, volcanic glass, and radiolarians are also present. The transition from Unit II to Unit III is gradual.

Unit III

Interval: 199-1222A-7H-4, 130 cm, through 8H-3, 115 cm
Depth: 58.7–66.6 mbsf
Age: middle Eocene to early Eocene
Lithology: iron oxide clay with zeolites

Unit III is dominated by clay with iron oxides and zeolites. Sediments are dark brown (10YR 3/3) and slightly mottled with yellowish brown (10YR 5/6). Iron oxide minerals comprise a significant proportion of the sediment, up to 35% in some samples. Minor constituents include zeolites, opaque minerals, and trace amounts of rhombohedral dolomite crystals. The basal contact of Unit III is obscured by sediment flow-in. At Hole 1222B, drilling was terminated at 64.4 mbsf and only the upper portion of Unit III was recovered.

Unit IV

Interval: 199-1222A-8H-3, 115 cm, through 12X-CC, 4 cm
Depth: 66.6–97.7 mbsf
Age: early Eocene
Lithology: chert

Sediments comprising Unit IV were poorly recovered by drilling and are represented by a few small angular chert fragments recovered in the core catchers of the XCB. The uppermost 5.4 m of this unit (interval 199-1222A-8H-3, 155 cm, through 8H-CC) are highly disturbed by flow-in consisting of small chert fragments mixed with sediments from Unit III. The Unit III–IV transition was placed at the top of the flow-in disturbance because this is probably the depth at which chert was first encountered. Chert fragments are black (N1) and exhibit thin, very dark brown (10YR 2/2) laminations. Just above basement, a large chert nodule rimmed with very pale brown (10YR 8/2) nannofossil chalk provides a datum that indicates early Eocene age (Subzone CP9a [NP10]) (see **"Calcareous Nannofossils,"** p. 7, in "Biostratigraphy"). A few small fragments of claystone are also mixed with chert breccia near the base of Section 199-1222A-12X-CC.

Unit V

Interval: 199-1222A-12X-CC, 4–45 cm
Depth: 97.7–97.8 mbsf
Age: early Eocene
Lithology: basalt

Core 199-1222A-12X contains a fine-grained, weathered ocean-floor basalt with aphanitic texture and a glassy rim. Fragments are highly altered and show light greenish gray color (5YG 7/1).

Discussion/Summary

The sedimentary section at Site 1222 is dominated by chert and clay-rich lithologies. Nannofossils scraped from the rim of one chert fragment recovered directly above basement basalt suggest sedimentation began during the early Eocene at ~53.5 Ma. Basal sediments at this site are poorly represented but probably include carbonate chalk and claystone lithologies, based on the few fragments recovered with chert drilling breccia in Section 199-1222A-12X-CC and at other Leg 199 drill sites. Sedimentation during the middle Eocene was dominated by clay, probably eolian transported. However, hydrothermal sources may have contributed a substantial amount of material to this site as suggested by the increased amount of iron oxide minerals (35%) compared to other sites. Sediments gradually shift in composition from clay to nannofossil ooze across the Eocene/Oligocene (E/O) boundary interval, a lithologic change that is likely related to the global deepening of the calcite compensation depth in the early Oligocene (van Andel et al., 1975).

Miocene and younger sedimentation is dominantly zeolitic clay. During the Pliocene, however, diatoms become an important sedimentary component and sometimes are present as laminated intervals of diatom ooze, presumably associated with the rapid deposition of large "algal mats." Such events have been observed in the modern Pacific (Barber, 1992) and in Neogene sedimentary records from Ocean Drilling

Program Leg 138 (Kemp et al., 1995). The depositional model proposed for laminated diatom intervals suggests algal mats may represent regions near strong oceanic frontal boundaries. This would suggest that a water-mass boundary may have been present near 13°N above Site 1222 during the Pliocene.

Clay once again dominates the sequence in sediments younger than the Pliocene. More than 16 m of clay was deposited since the late Pliocene. Typically, pelagic clays accumulate at much slower rates, thus, sediment reworking in this portion of the sequence seems likely (see **"Radiolarians,"** p. 8, in "Biostratigraphy").

BIOSTRATIGRAPHY

Radiolarians provide the biostratigraphic framework for Site 1222. Planktonic foraminifers are completely dissolved in all samples investigated. Calcareous nannofossils of early Oligocene age are present in one short interval in Core 199-1222A-7H, and early Eocene calcareous nannofossils are present in chalk attached to a piece of chert in Section 199-1222A-12X-CC.

The biostratigraphic distribution of radiolarians suggests massive reworking and mixed Pliocene assemblages in the uppermost two and a half cores, between 0 and 21 mbsf (Fig. F5). The following two cores, between ~21 and 40 mbsf, contain upper and lower Miocene radiolarian assemblages. Two cores between ~40 and 60 mbsf contain upper and lower Oligocene radiolarian assemblages. Nannofossils are present between ~55 and 60 mbsf, supporting the radiolarian biostratigraphy. This upper part of the section at Site 1222 appears to contain several breaks in sedimentation. Unlike other Leg 199 sites, at Site 1222 a major hiatus is present between earliest Oligocene and middle Eocene time, having a duration on the order of ~5–6 m.y.

F5. Calcareous and siliceous biostratigraphy, p. 22.

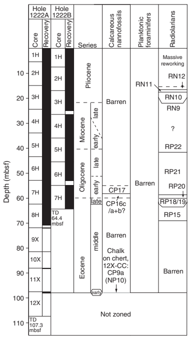

Calcareous Nannofossils

Calcareous nannofossils are present from Sample 199-1222A-7H-2, 60 cm, through 7H-CC. Sample 199-1222A-7H-2, 60 cm, contains a severely reduced, dissolution-biased assemblage with remains of *Dictyoccites hesslandii, Sphenolithus moriformis,* and distal shield rims of *Coccolithus pelagicus. Discoaster deflandrei, Discoaster nodifer,* and *Discoaster tanii* are also present; most specimens show calcite overgrowth. The uppermost occurrence of *Reticulofenestra umbilicus* is observed between Samples 199-1222A-7H-4, 60 cm, and 7H-4, 84 cm. It follows that the transition from nannofossil-bearing sediment to the overlying barren sediment in Core 199-1222A-7H is present just above the CP16c/CP17 (NP22/NP23) zonal boundary.

Nannofossil assemblages are increasingly dissolved through Section 199-1222A-7H-5. Samples 199-1222A-7H-5, 5 cm, and 7H-5, 50 cm, can be referred to Subzone CP16c (NP22), whereas the nannofossils in Sample 199-1222A-7H-5, 100 cm, are too dissolved to say with any confidence whether this sample belongs to Subzone CP16c or CP16a+b (NP21). Sample 199-1222A-7H-5, 147 cm, only contains discoasters, but none of these are the exclusively Eocene forms that characterize Zone CP15 (NP20). Core 199-1222A-7H is barren of calcareous nannofossils below Sample 199-1222A-7H-5, 147 cm, although the core catcher sample contains isolated contaminated pieces of nannofossil ooze belonging to the overlying Oligocene Subzone CP16c (NP22).

Chalk attached to a piece of chert in Section 199-1222A-12X-CC contains nannofossils representing lowermost Subzone 9a (NP10) of the lower Eocene. The assemblage of this sample includes overgrown specimens of *Tribrachiatus bramlettei,* together with *Chiasmolithus bidens, C. pelagicus, Discoaster mohleri, Discoaster multiradiatus, Discoaster nobilis, Ericsonia* spp., *Neochiastozygus junctus, Neocrepidolithus* spp., *Placozygus sigmoides, Prinsius bisulcus, Sphenolithus primus,* and *Toweius pertusus.*

Planktonic Foraminifers

Planktonic foraminfers were not found in any core catcher samples from Site 1222.

Benthic Foraminifers

Core catcher samples from Cores 199-1222A-1H through 12X are barren of benthic foraminifers. However, benthic foraminifers were found at one horizon in Hole 1222B. Sample 199-1222B-1H-CC contains a benthic foraminiferal assemblage characterized by *Siphonodosaria abyssorum, Cibicidoides mundulus, Gyroidinoides soldanii,* and *Oridorsalis umbonatus. C. mundulus* is a long-ranging species from late Oligocene to Pleistocene, and this species is abundant at bathyal and abyssal paleodepths (van Morkhoven et al., 1986). This assemblage shows moderate preservation.

Radiolarians

T2. Summary of radiolarian zonal boundary ages, p. 41.

T3. Radiolarian zonal boundaries, p. 44.

The preservation and abundance of radiolarians at this site varied considerably both downhole and within individual cores (Table T2). Reworking of Eocene and Oligocene taxa plus a number of hiatuses within the sedimentary sequence made zonal designation difficult. Zonal boundaries for radiolarians at Site 1222 are listed in Table T3.

Although Cores 199-1222A-1H and 2H contain a few moderately well preserved forms, it was not possible to assign an age to the material. It is probably Quaternary but with an admixture of Eocene and Oligocene. Several samples were taken from within Core 199-1222A-3H on either side of the diatom mats noted by the sedimentologists (see **"Subunit IA,"** p. 4, in "Lithostratigraphy"). Along with reworked Eocene species, Sample 199-1222A-3H-2, 14–16 cm, contains a mixed assemblage of species indicative of the Pliocene. The presence of *Pterocanium prismatium, Anthocyrtidium angulare,* and *Lamprocyrtis nigriniae* suggest Zone RN12, but *Stichocorys peregrina* is also present, which suggests Zone RN11 or older. Sample 199-1222A-3H-2, 14–16 cm, and subsequent Core 199-1222A-3H samples all contain an abundance of fragments of the diatom *Ethomodiscus rex*. An age assignment of Zone RN10 is clearer for Samples 199-1222A-3H-2, 110–112 cm; 3H-3, 42–44 cm; and 3H-4, 18–20 cm, with a greater abundance of species such as *S. peregrina, Spongaster tetras tetras,* and *P. prismatium* amidst the ever-present reworked Eocene species. We have assigned an age of Zone RN9 to Sample 199-1222A-3H-4, 88–90 cm, because of the presence of *Didymocyrtis penultima,* the last presence of which marks the RP9/RP10 zonal boundary. Samples from the above-described interval represent the only Pliocene material found during Leg 199.

The next downhole sample for which it is possible to determine an age is Sample 199-1222A-5H-6, 45–47 cm. It belongs to uppermost Oligocene Zone RP22, based on the presence of *Lychnocanoma elongata* and the absence of *Cyrtocapsella tetraperam,* but also contains a large amount of reworked Eocene material. Sample 199-1222A-5-CC belongs to Zone RP21. The sample also contains a large number of orosphaerids and, once again, a reworked Eocene fauna. Core 199-1222A-6H and the upper three sections of Core 199-1222A-7H contain only trace amounts of non–age diagnostic radiolarians. Abundance and preservation improves slightly in Samples 199-1222A-7H-4, 45–47 cm, and 7H-5, 45–47 cm. Based on the presence of *Dorcadospyris spinosa, Dorcadospyris quadripes,* and *Theocyrtis tuberosa,* we assigned an age of Zone RP20 to these samples, despite the absence of *Lithocyclia angusta*. In Sample 199-1222A-7H-6, 45–47 cm, it becomes more difficult to distinguish reworked specimens from in-place fauna. The rare and poorly preserved specimens suggest an age of Zone RP18 or younger. Data from the nannofossil assemblage in Sample 199-1222A-7H-5, 100 cm, indicate that an age younger than Zone RP18 is appropriate. There is an ~6-m.y. hiatus before Sample 199-1222A-7H-7, 66–68 cm, which clearly belongs to Zone RP15 as do subsequent downhole samples (199-1222A-7H-CC; 8H-2, 45–46 cm; and 8H-3, 45–47 cm). The rest of the recovered material in Hole 1222A is barren of radiolarians or contains only trace amounts of non–age diagnostic forms.

Material recovered from Hole 1222B shows a similar pattern of disjointed ages, preservation, and radiolarian abundance. Sample 199-1222B-1H-CC contains an abundance of reworked Eocene fauna along with rare late Neogene forms such as *Theocorythium vetulum, Didymocyrtis tetrathalamus,* and *Lamprocyrtis heteroporos*. Samples from 199-1222B-2H-4, 36–38 cm; 2H-5, 43–45 cm; and 2H-CC probably belong to Zone RP11. In Samples 199-1222B-5H-CC, 6H-CC, and 7H-3, 45–47 cm, the fauna indicates an age of Zone RP21. Sample 199-1222B-5H-CC is particularly rich in orosphaerids. The remaining downhole samples (199-1222B-7H-5, 100–102 cm; 7H-6, 44–46 cm; and 7H-CC) all could be placed in Zone RP20.

PALEOMAGNETISM

All APC cores from Holes 1222A and 1222B that did not show a large drilling-related disturbance were measured on the shipboard pass-through cryogenic magnetometer. Natural remanent magnetization (NRM) was measured at 5-cm intervals in each core section, followed by three steps of alternating-field (AF) demagnetization up to a maximum peak field of 20 mT. In addition to whole long-core measurements, discrete samples were taken from Hole 1222A to carry out more detailed progressive demagnetization and rock-magnetic analysis.

F6. Magnetization intensities after AF demagnetization, p. 23.

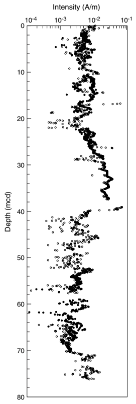

The NRM intensities were in the order of 10^{-1} to 10^{-2} A/m and decreased to ~10^{-2} to 10^{-3} A/m after partial AF demagnetization (Fig. F6). The drilling-induced overprint was mostly removed by AF demagnetization at 10 mT. Yet, a large group of ChRM directions show relatively high magnetic inclinations after blanket demagnetization, especially in the most clay-rich lithologic units. The cause of the steep inclinations is unclear and might be indicative of unrecognized deformation caused by drilling. We noticed that cores (e.g., 199-1222A-4H) with bedding features or burrows show that the sediment has been deformed near the core wall edges or "core liner."

The paleomagnetic data from lithologic Subunit IA down to ~40 mbsf are not interpretable except for the very top of Hole 1222A. Core 199-1222A-4H displays a subvertical magnetic inclination, which is clearly not a record of the paleomagnetic field. We suspect that core deformation is responsible for such a distribution of magnetization directions. Other cores from both Holes 1222A and 1222B also show variable degrees of disturbance, mostly related to flow-in, and have not been considered for further paleomagnetic analysis.

Sediments in lithologic Subunit IB provided identifiable paleomagnetic polarity reversals. A preliminary correlation of the magnetic stratigraphy to the geomagnetic polarity timescale is shown in Figure **F7.** At the very top of the section, we were able to identify the bottom of polarity Chron C1n (Brunhes). Stratigraphically downward, we identify Chrons C6Cn to (?)C12n. A long reversed-magnetization chron at the bottom of the section (~67 to 75 mcd) (Fig. **F7**) could represent Chron C18r, as Zone RP15 (middle Eocene) is found starting at ~66 mcd (see **"Radiolarians,"** p. 8, in "Biostratigraphy") and downhole.

COMPOSITE DEPTHS

Site 1222 extended to a total depth of 98.15 mbsf (Core 199-1222A-12X), with good recovery down to a depth of 71.13 mbsf (Core 199-1222A-8H). Below this depth, only chert and basalt were recovered. Similar to Site 1221, cores recovered from Site 1222 frequently showed evidence of flow-in, attributed to strong heave motions during coring. The predominantly clay and radiolarian clay found at Site 1222 showed signs of significant expansion during coring, which resulted in longer than average gaps between consecutive cores. Thus, although overlap between the two adjacent drilled holes was good, it was difficult to generate a complete and continuous record.

A composite section was constructed for the upper 80 mcd of Site 1222 using multisensor track (MST) and color reflectance data to determine depth offsets between cores from Holes 1222A and 1222B (Fig. **F8**). Magnetic susceptibility (MS), *P*-wave velocity, natural gamma ray (NGR), and color reflectance data were collected at 2-cm intervals and GRA bulk density at 4-cm intervals in all APC cores. Disturbed intervals, as determined by visual inspection of split cores, are listed in Table **T4.** Data from these intervals were removed prior to correlation work. Table **T5** lists the offsets that were applied to cores from each hole to create a composite depth record.

It was possible to construct a continuous spliced record from Site 1222 down to the base of Core 199-1222A-4H (34.44 mbsf; 37.88 mcd), below which it was possible to align most cores from the two drilled holes to each other but without continuous overlap. As many intervals in Hole 1222B showed flow-in and had to be removed prior to correlation, data from below Core 199-122A-4H were merely appended to the splice. Exceptions to this are Cores 199-1222A-7H and 199-1222B-7H, which showed good overlap and allowed the splicing of an additional ~13 m from ~59 to 72 mcd.

Figure **F9** shows the resulting spliced records for GRA bulk density, MS, and color reflectance (splice tie points for Site 1222 are given in Table **T6**). The unusual MS profile bears resemblance to that obtained from Site 1215. Together with age control provided by biostratigraphic datums (see **"Biostratigraphy,"** p. 7), this might allow further correlation between sites.

F7. Composite magnetic stratigraphy, p. 24.

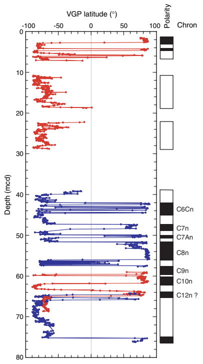

F8. GRA bulk density, magnetic susceptibility, and color reflectance data plotted vs. composite depth, p. 25.

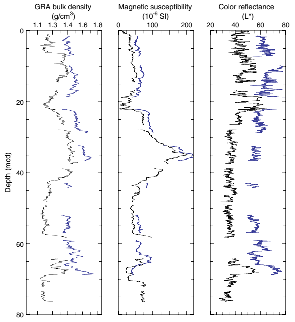

T4. Core disturbance intervals, p. 45.

T5. Core composite depth offsets, p. 46.

F9. Spliced records of GRA bulk density, magnetic susceptibility, and the color reflectance parameter, p. 26.

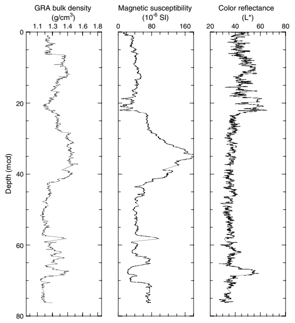

T6. Splice tie points, p. 47.

SEDIMENTATION AND ACCUMULATION RATES

The radiolarian stratigraphy, together with a set of 21 paleomagnetic reversals, is defined in Holes 1222A and 1222B (Tables T7, T8). These stratigraphies are used to calculate the average linear sedimentation rates (LSRs) for Site 1222 through the section, with dependence on two nannofossil events providing age constraints near the base of the Oligocene and the base of the section (Fig. F10; Table T8). The paleomagnetic stratigraphy extends through the section recovered by APC coring (0–81 mcd). At the base of the Oligocene in Core 199-1222A-7H, there is a marked hiatus as the radiolarian assemblage (although poorly preserved and containing reworked older specimens) shows a transition from the lower Oligocene Zone RP20 in Section 199-1222A-7H-5 through a poorly preserved upper Eocene interval in Section 7H-6, to a well-preserved middle Eocene assemblage (Zone RP15) in Section 7H-7 (see **"Biostratigraphy,"** p. 7). The age of the base of the hole is based on the identification a nannofossil assemblage from Zone NP10, recovered from the crust of a piece of chert in Section 199-1222A-12X-CC (Tables T7, T8).

There is no site survey piston core from Site 1222; however, the piston Core EW9709-14P (Lyle, 2000), taken at the next closest site (Site 1221), can be correlated to the density record of Site 1222 (Fig. F11). This correlation is consistent with radiolarian biostratigraphy in the piston core and at Site 1222. Unlike Site 1221, Site 1222 has a fairly thick interval of siliceous clays overlying the high-amplitude density variations found in the lower Oligocene section of lithologic Units II and III (see **"Lithostratigraphy,"** p. 4). The section in the piston core equivalent to lithologic Unit I in Site 1222 is represented by 4.5 m of pelagic red clay showing none of the density variations seen in Site 1222 (Fig. F11; see **"Lithostratigraphy,"** p. 4).

Based on a simple linear interpolation through the uppermost stratigraphic events (Tables T7, T8), the siliceous clays of the upper part of lithologic Subunits IA (see **"Lithostratigraphy,"** p. 4) have an LSR of about 5.5 m/m.y. Below this relatively high LSR of the Pliocene–Quaternary section, the rates decrease markedly through the Miocene (Fig. F10). Starting in the Oligocene (top of Chron C7n; Tables T7, T8), the LSR generally increases, reaching 3–6 m/m.y. in the Oligocene. Part of the base of the Oligocene may be missing in the hiatus interval that spans the E/O boundary, giving rise to the relatively low LSR (1.75 m/m.y.) in the lower Oligocene. Below the hiatus zone down to the base of the section, the LSR is estimated to be ~1.45 m/m.y.

LSR values may be combined with the dry bulk density (DBD) data from porosity measurements on individual samples (see **"Physical Properties,"** p. 13) (Table T12) to determine the bulk mass accumulation rates (MARs) of the sediments (Table T9). Sediment with an LSR of 1.0 cm/k.y. and a DBD of 1.0 g/cm³ will have an MAR value of 1.0 g/cm²/k.y. The observed values are rarely this high, so we report the data in milligrams per square centimeter per thousand years (mg/cm²/k.y.) (Fig. F12). MAR values are relatively high in the Pliocene sediments of Subunit IA (>250 mg/cm²/k.y.). These are the highest MAR values for the young part of the section seen at any of the Leg 199 sites. The lower portion of Subunit IA has lower flux values of 60–80 mg/cm²/k.y. The radiolarian clays of Subunit IB accumulated at a modest rate of ~150 mg/cm²/k.y. The lower Oligocene nannofossil ooze of Unit II displays flux values of only 50–100 mg/cm²/k.y., al-

T7. Paleomagnetic events, p. 48.

T8. Nannofossil and radiolarian events, p. 49.

F10. LSRs and chronostratigraphic markers, p. 27.

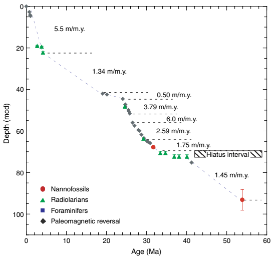

F11. Density record of site survey piston Core EW9709-14P compared to density record of Site 1222, p. 28.

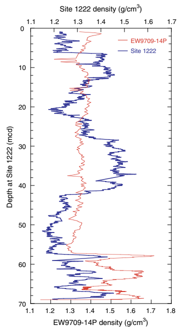

T9. Depths, ages, rates, and fluxes of sediments, p. 50.

F12. Mass accumulation rates of sediments, p. 29.

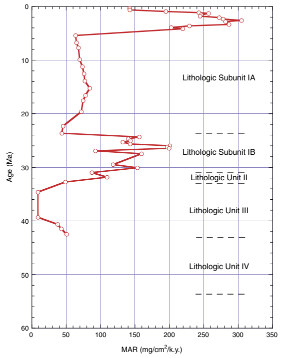

though data are few for this horizon. Unit III, a clay layer, accumulated quite slowly and may contain, or record, a significant hiatus. There are no data relevant to determination of fluxes in the chert horizon of Unit IV.

GEOCHEMISTRY

Interstitial Water Geochemistry

We collected interstitial waters from Hole 1222A from one sample from every core for the first six cores at depths ranging from 2.95 to 47.85 mbsf (Table T10; Fig. F13).

T10. Interstitial water data, p. 51.

F13. Interstitial water data, p. 30.

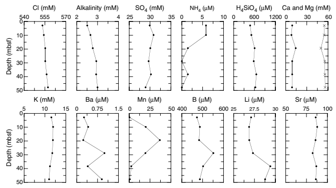

Chlorinity, as measured by titration, increases with depth from 553 mM at 2.95 mbsf to 557 mM at 47.85 mbsf (Fig. F13). Sodium concentrations (determined by charge balance) are, on average, 1.6% higher than those measured by ion chromatograph. Sodium concentrations generally remain steady at values similar to that of average seawater. Salinity, as measured by a handheld refractometer, increases with depth from 34.5 at 2.95 mbsf to 35.0 at 47.85 mbsf.

Alkalinity increases with depth from 2.51 mM at 2.95 mbsf to 3.00 mM at 47.85 mbsf. The pH varies between 6.98 and 7.13. Like all other Leg 199 sites, average sulfate concentrations are high (30.0 mM) and ammonium concentrations are low (≤6 µM), indicating little oxidation of organic matter.

Dissolved silica concentrations increase slightly with depth, from 474 µM at 2.95 mbsf to ~628 µM at 47.85 mbsf. These interstitial water silica values are consistent with dissolution of biogenic silica.

Calcium and magnesium show little evidence of basement alteration. Calcium and magnesium concentrations are relatively constant downcore (9 and 55 mM, respectively), except for one sample at 19.35 mbsf, which has relatively high Ca (14 mM) and low magnesium (50.1 mM) concentrations. Potassium concentrations decrease slightly downsection from ~12 to 11 mM. Lithium concentrations increase slightly downsection, from ~27 to 29 µM.

Strontium concentrations remain at values similar to seawater throughout the record, consistent with the low levels of carbonate in these sediments. Dissolved manganese increases from ~0 µM at 2.95 mbsf to ~40 µM at the level of the calcium maxima and the magnesium minima (19.35 mbsf) and subsequently decreases to negligible values at 47.85 mbsf. Barium is low throughout the profile (≤1 µM). Levels of dissolved boron are slightly higher than average seawater (416 µM). Boron concentrations increase from ~472 µM at 2.95 mbsf to ~552 µM at 28.85 mbsf and subsequently decrease to ~487 µM at 47.85 mbsf (Table T10).

In summary, the pore water profiles from Site 1220 primarily reflect minor organic matter degradation and the dissolution of biogenic silica. Most of the dissolved chemical constituents show a lack of gradient with depth and values similar to or slightly higher than seawater.

Solid-Phase Geochemistry

We collected bulk-sediment samples in every other section, adjacent to the interval sampled for physical properties (see "Physical Properties," p. 13) at Site 1222, resulting in a sampling resolution of approximately three samples per core. The bulk inductively coupled plasma–

atomic emission spectroscopy data from Site 1222 is suspect because of excessively high levels of drift during the run. This resulted in very poor precision for most elements (e.g., Ba = 26%, Ca = 34%, Fe = 79%, Mn = 32%, Si = 22%, and Sr = 85%). For this reason, we do not report the data. The poor precision for Site 1222 data probably results from excessive ship motion during sample weighing and analyses (see **"Geochemistry,"** p. 20, in the "Explanatory Notes" chapter for more discussion).

Calcium carbonate ($CaCO_3$) (in weight percent) was determined by coulometric methods for two to three samples per core from 2.24 to 64.63 mbsf for Site 1222 (Table **T11;** Fig. **F14**). $CaCO_3$ is low (<1 wt%) in Unit I and is moderate in the nannofossil ooze of Unit II (40–67 wt%). Organic carbon (in weight percent) determined for one sample per core is uniformly low (<0.15 wt%).

T11. $CaCO_3$ and C_{org} data, p. 52.

F14. $CaCO_3$ data, p. 31.

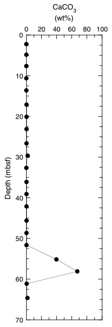

PHYSICAL PROPERTIES

Physical properties at Site 1222 were measured on whole cores, split cores, and discrete samples. MST measurements (bulk density, MS, *P*-wave velocity, and natural gamma radiation) and thermal conductivity comprised the whole-core measurements. Compressional wave velocity measurements on split cores and moisture and density (MAD) analyses on discrete core samples were made at a frequency of one per undisturbed section in Hole 1222A. Light absorption spectroscopy (LAS) analyses were performed on the MAD samples as well as an additional one sample per section (located ~50 cm from the MAD sample).

Density and Porosity

Two methods were used to evaluate the wet bulk density at Site 1222. Gamma ray attenuation (GRA) provided an estimate from whole cores. MAD samples gave a second, independent measure of wet bulk density, along with providing DBD, grain density, water content, and porosity from discrete samples (Table **T12**). The GRA and MAD wet bulk densities are a close match throughout the interval of core recovery in Hole 1222A (Fig. **F15**), with the exception of the interval from 6.90 to 14.40 mbsf (Sections 199-1222A-2H-2 through 2H-6). This interval contains a recurrence of the electronic artifact in the MST data acquisition that first appeared at Site 1220. The displacement is not present in the Hole 1222B GRA record, and, as at Sites 1220 and 1221, the appearance of Sections 199-1222A-2H-2 through 2H-6 does differ from that of adjacent sediments. Crossplots of wet bulk density and DBD vs. interpolated GRA bulk density, which exclude data from the sections in question, display an excellent correlation between the two bulk density measures (Fig. **F16**).

T12. Moisture and density measures, p. 53.

F15. Moisture and density measurements, p. 32.

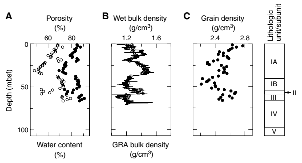

The wet bulk density at the top of lithologic Unit I (0–40.5 mbsf) is 1.27 g/cm³. As the clays that comprise the unit compact, wet bulk density increases with depth, reaching a maximum of 1.46 g/cm³ at 31.15 mbsf. The downhole trend of increasing density is interrupted between 16.8 and 20.2 mbsf by an interval of low-density (1.23–1.27 g/cm³) diatom ooze (see **"Unit I,"** p. 4, in "Lithostratigraphy"). The small-scale variation in bulk density that accompanies alternating lithologies in Subunit IA is demonstrated by low density in diatom-rich sediments and higher density in clayey intervals in Core 199-1222A-3H (Fig. **F17**). A sharp decrease in wet bulk density to ~1.25 g/cm³ is present in the lowermost part of Subunit IA. The bulk density remains at this level, av-

F16. Wet and dry bulk density plotted with GRA density, p. 33.

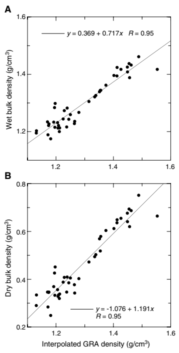

eraging 1.24 g/cm³, in the radiolarian clay of Subunit IB (40.5–54.9 mbsf). Wet bulk density increases sharply to 1.40 g/cm³ at the top of Unit II (58.7–66.6 mbsf) and remains at roughly this level throughout the nannofossil ooze of this unit. A rapid decrease in bulk density to 1.20 g/cm³ marks the top of lithologic Unit III (58.7–66.6 mbsf), and wet bulk density averages 1.21 g/cm³ for the clays in this unit.

F17. Comparison of MS, GRA density, velocity, and NGR with digital core images, p. 34.

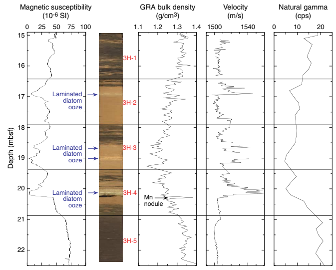

Grain density varies over a wide range (2.21–2.77 g/cm³) at Site 1222 as a result of the combination of different lithologies (Fig. **F15**). The grain density is roughly 2.60–2.65 g/cm³ at the top of Unit I, reflecting the predominance of clay. Higher grain densities, up to 2.77 g/cm³ at 2.25 mbsf, possibly reflect the presence of manganese oxide and other opaque sediment constituents (see **"Unit I,"** p. 4, in "Lithostratigraphy"). Grain density decreases downhole to 2.30 g/cm³ at 21.65 mbsf in the clay below the diatom ooze in Subunit IA. Below 21.65 mbsf, grain density increases and is ~2.53 g/cm³ between 25 and 35 mbsf. The density is lower at the base of Subunit IA (2.36 g/cm³) in the transition to the radiolarian clay of Subunit IB. Grain density in Subunit IB ranges from 2.21 to 2.52 g/cm³, with the highest densities at the base of the unit. Grain density in the underlying nannofossil ooze of Unit II varies in a narrow range about an average of 2.65 g/cm³. Grain density decreases in the Unit III clay, ranging from 2.45 to 2.63 g/cm³ and averaging 2.52 g/cm³.

Sediment porosity near the seafloor at Site 1222 is 85%. A downhole trend of decreasing porosity, to 69% at 31.15 mbsf, is interrupted by the high-porosity (85%) diatom ooze between 16.8 and 20.2 mbsf (Fig. **F15**). Below 31.15 mbsf, porosity in the Unit I clays increases with depth to 84% at 39.15 mbsf. Most of Subunit IB has a porosity of ~86%. The porosity of the radiolarian clays decreases at the base of the unit in the transition to the lower-porosity (~75%) nannofossil ooze of Unit II. Porosity increases sharply to 88% at the top of Unit III and remains roughly at this level throughout the unit.

LAS

LAS studies were conducted on sediments from Hole 1222A at a frequency of two samples per undisturbed section (see **Vanden Berg and Jarrard,** this volume, for a discussion of the LAS technique). Samples were not collected below 66.2 mbsf because of poor core recovery. Semiquantitative mineral concentrations were calculated from the collected spectra, assuming a four-component system: calcite, opal, smectite, and illite (Table **T13**).

T13. LAS-based mineralogy, p. 54.

Calcite is overestimated throughout Site 1222 because of the lightness of the material (Fig. **F18**). The high concentrations of zeolites may be contributing to this light color. Overall, the clay intervals show high concentrations of smectite and illite and also correspond to areas of low opal. The illite–smectite transition is found in the upper 10 m of sediment. The diatom ooze (~17 mbsf) shows a large drop in clay and an increase in opal as well as the radiolarian ooze of Subunit IB. The nannofossil ooze of Unit II is associated with the expected high calcite values (up to 80%). Postcruise work will involve a recalculation of these concentrations using better quality standards. This should eliminate the overestimated calcite and the variability in the illite values.

F18. LAS mineralogy determinations, p. 35.

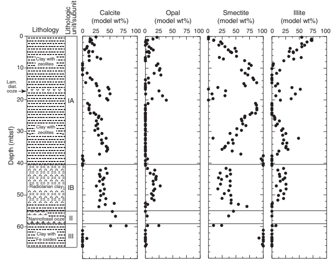

Compressional Wave Velocity

Compressional wave velocity was measured by the *P*-wave logger (PWL) on all whole cores from Holes 1222A and 1222B. The insertion and contact probe systems were used to measure velocities on split cores from Hole 1222A (Table **T14**). Agreement between PWL and split-core velocities is good, typically displaying offsets of <10 m/s (Fig. **F19**). The difference between the whole-core and split-core velocities is greater in the radiolarian clay between 50 and 52 mbsf, where contact probe velocities are ~30 m/s higher than the PWL velocities. This disparity in velocities in radiolarian clay and ooze is present at other Leg 199 sites and possibly results from dewatering of the radiolarian-rich sediment after core splitting.

T14. Split-core velocity measurements, p. 55.

F19. Compressional wave velocity, p. 36.

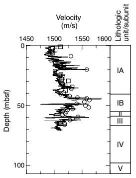

Velocity varies with lithology at Site 1222 (Fig. **F19**). In the Subunit IA clay, transverse velocity is 1510 m/s near the seafloor and is at a maximum of 1558 m/s in the diatom ooze at 20.11 mbsf. The velocity variation that accompanies alternating lithologies in Subunit IA is displayed in the PWL record for Core 199-1222A-3H (Fig. **F17**), in which peaks in velocity correspond to layers of laminated diatom ooze and lower velocities are present in clay intervals. Velocity increases slightly with depth in Subunit IA and is ~1520 m/s at the base of the unit. In Subunit IB velocity is 1512 m/s at 40.66 mbsf and rapidly increases to 1563 m/s at 45.66 mbsf. Below this depth, velocity decreases downhole and is 1524 m/s at the base of the unit. Overall, the average velocity for the radiolarian clay of Subunit IB is 1543 m/s. The downhole decrease in velocity continues in the nannofossil ooze of Unit II. The average velocity for this unit is 1519 m/s. Velocity sharply increases to 1543 m/s at the top Unit III. It decreases with depth in the clay of Unit III to 1519 m/s at 66.16 mbsf, just above the base of the unit.

Velocity anisotropy was determined with the contact probe system to evaluate changes in fabric that might accompany sediment burial. The clays of Subunit IA are nearly isotropic with a range in anisotropy from 0.6% to 2.0% without a downhole trend, suggesting that little particle reorientation has occurred (Table **T14**).

Thermal Conductivity

T15. Thermal conductivity, p. 56.

Thermal conductivity was measured on the third section of all undisturbed cores from Holes 1222A and 1222B (Table **T15**). Overall, the conductivity of sediments recovered at Site 1222 is low, ranging from 0.69 to 0.82 W/(m·K). Near the top of Subunit IA, thermal conductivity is 0.72 W/(m·K) (Fig. **F20**). It increases downhole in the clay to 0.82 W/(m·K) at 28.16 m/s. This increase accompanies the downhole decrease in porosity. Thermal conductivity decreases to 0.73 W/(m·K) near the base of Subunit IA as porosity increases in transition to the radiolarian clay of Subunit IB. The high-porosity radiolarian clay of Subunit IB has the lowest conductivity at Site 1222, averaging 0.71 W/(m·K). Below the radiolarian clay, thermal conductivity increases to an average of 0.78 W/(m·K) in the nannofossil ooze of Unit II. As porosity increases in the clay of Unit III, thermal conductivity decreases to 0.71 W/(m·K) at 66.16 mbsf.

F20. Thermal conductivity, p. 37.

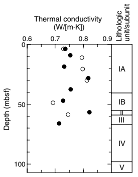

Natural Gamma Radiation

Natural gamma radiation was measured on all whole cores from Holes 1222A and 1222B (Fig. **F21**). The NGR values are as high as 137.1

F21. Natural gamma radiation, p. 38.

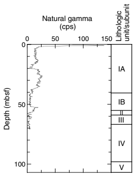

counts per second (cps) at 1.0 mbsf before they decrease to an average of 19.8 cps for the rest of Subunit IA. Between 16.8 and 20.2 mbsf, natural gamma radiation values decrease to an average of 8.0 cps in the interval of diatom-rich sediments. Within this interval, thin layers of laminated diatom ooze are present, which record minima in NGR values (Fig. **F17**). In the upper radiolarian-rich part of Subunit IB (40.5–52.1 mbsf), NGR values decrease to an average of 5.4 cps. The lower section of Subunit IB (52.6–56.5 mbsf) records a rise in values to an average of 12.6 cps and correlates to an interval of more clay-rich sediments. Below 56.5 mbsf, NGR values decrease downcore to near background levels.

MS

Whole-core MS measurements were made on all cores from Holes 1222A and 1222B (Fig. **F22**) and correlate well with other physical property measurements. MS values in the upper section of Subunit IA (0.0–16.8 mbsf) average 40 × 10^{-6} SI, followed by a decrease between 16.8 and 20.4 mbsf to an average of 24 × 10^{-6} SI. This low-susceptibility interval correlates with the zone of diatom-rich sediments. Within this interval, lower than average susceptibility (as low as 3 × 10^{-6} SI) correlates with thin layers of laminated diatom ooze (Fig. **F17**). The lower part of Subunit IA (20.4–40.5 mbsf) is characterized by a broad peak in susceptibility, with values as high as 202 × 10^{-6} SI at 31.5 mbsf. Between 40.5 and 52.1 mbsf in the radiolarian-rich interval of Subunit IB, susceptibility decreases to an average of 45 × 10^{-6} SI before increasing again to an average of 73 × 10^{-6} SI in the clay-rich interval at the base of Subunit IB and the top of Unit II (52.1–56.5 mbsf) (see **"Subunit IB,"** p. 5, and **"Unit II,"** p. 5, both in "Lithostratigraphy"). Between 56.5 and 59.9 mbsf, MS decreases to an of average 29 × 10^{-6} SI in the nannofossil ooze. The clay-rich Unit III and top of Unit IV mark an increase in susceptibility to an average of 64 × 10^{-6} SI.

F22. Magnetic susceptibility, p. 39.

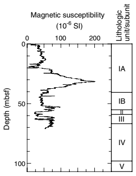

REFERENCES

Barber, R.T., 1992. Fall survey cruise finds cooling conditions in equatorial Pacific. *U.S. JGOFS News,* 4:1–6.

Cande, S.C., LaBrecque, J.L., Larson, R.L., Pitmann, W.C., III, Golovchenko, X., and Haxby, W.F., 1989. *Magnetic Lineations of the World's Ocean Basins.* AAPG Map Ser., 13.

Engebretson, D.C., Cox, A., and Gordon, R.G., 1985. *Relative Motions Between Oceanic and Continental Plates in the Pacific Basin.* Spec. Pap.—Geol. Soc. Am., 206.

Gripp, A.E., and Gordon, R.G., 1990. Current plate velocities relative to the hotspots incorporating the NUVEL-1 global plate motion model. *Geophys. Res. Lett.,* 17:1109–1112.

Kemp, A.E.S., Baldauf, J.G., and Pearce, RB, 1995. Origins and paleoceanographic significance of laminated diatom ooze from the eastern equatorial Pacific Ocean. *In* Pisias, N.G., Mayer, L.A., Janecek, T.R., Palmer-Julson, A., and van Andel, T.H. (Eds.), *Proc. ODP, Sci. Results,* 138: College Station, TX (Ocean Drilling Program), 641–645.

Lyle, M., 2000. Data submission to ODP Pollution Prevention and Safety Panel: proposed drill sites for ODP Leg 198—a Paleogene equatorial APC transect. *BSU-CGISS Tech Rept.,* 2000-03.

Sanfilippo, A., and Nigrini, C., 1996. Radiolarian biomarkers at the Oligocene/Miocene boundary. *In* Moguilevsky, A., Watley, R. (Eds.), *Microfossils and Oceanic Environments: Proc. ODP and the Mar. Biosphere Int. Conf.:* Aberystwyth, Wales (Univ. Wales, Aberystwyth Press), 317–326.

Sanfilippo, A., and Nigrini, C., 1998. Code numbers for Cenozoic low latitude radiolarian biostratigraphic zones and GPTS conversion tables. *Mar. Micropaleontol.,* 33:109–156.

Shackleton, N.J., Baldauf, J.G., Flores, J.-A., Iwai, M., Moore, T.C., Jr., Raffi, I., and Vincent, E., 1995. Biostratigraphic summary for Leg 138. *In* Pisias, N.G., Mayer, L.A., Janecek, T.R., Palmer-Julson, A., and van Andel, T.H. (Eds.), *Proc. ODP, Sci. Results,* 138: College Station, TX (Ocean Drilling Program), 517–536.

van Andel, T.H., Heath, G.R., and Moore, T.C., Jr., 1975. *Cenozoic History and Paleoceanography of the Central Equatorial Pacific Ocean: A Regional Synthesis of Deep Sea Drilling Project Data.* Mem.—Geol. Soc. Am., 143.

van Morkhoven, F.P.C.M., Berggren, W.A., and Edwards, A.S., 1986. *Cenozoic Cosmopolitan Deep-Water Benthic Foraminifera.* Bull. Cent. Rech. Explor.—Prod. Elf-Aquitaine, 11.

Figure F1. Location of Site 1222 in the Leg 199 transect. In the lower panel, gray shading = seafloor depths >5000 mbsl, red shading = approximate position of the nominal target crust of the 56-Ma transect.

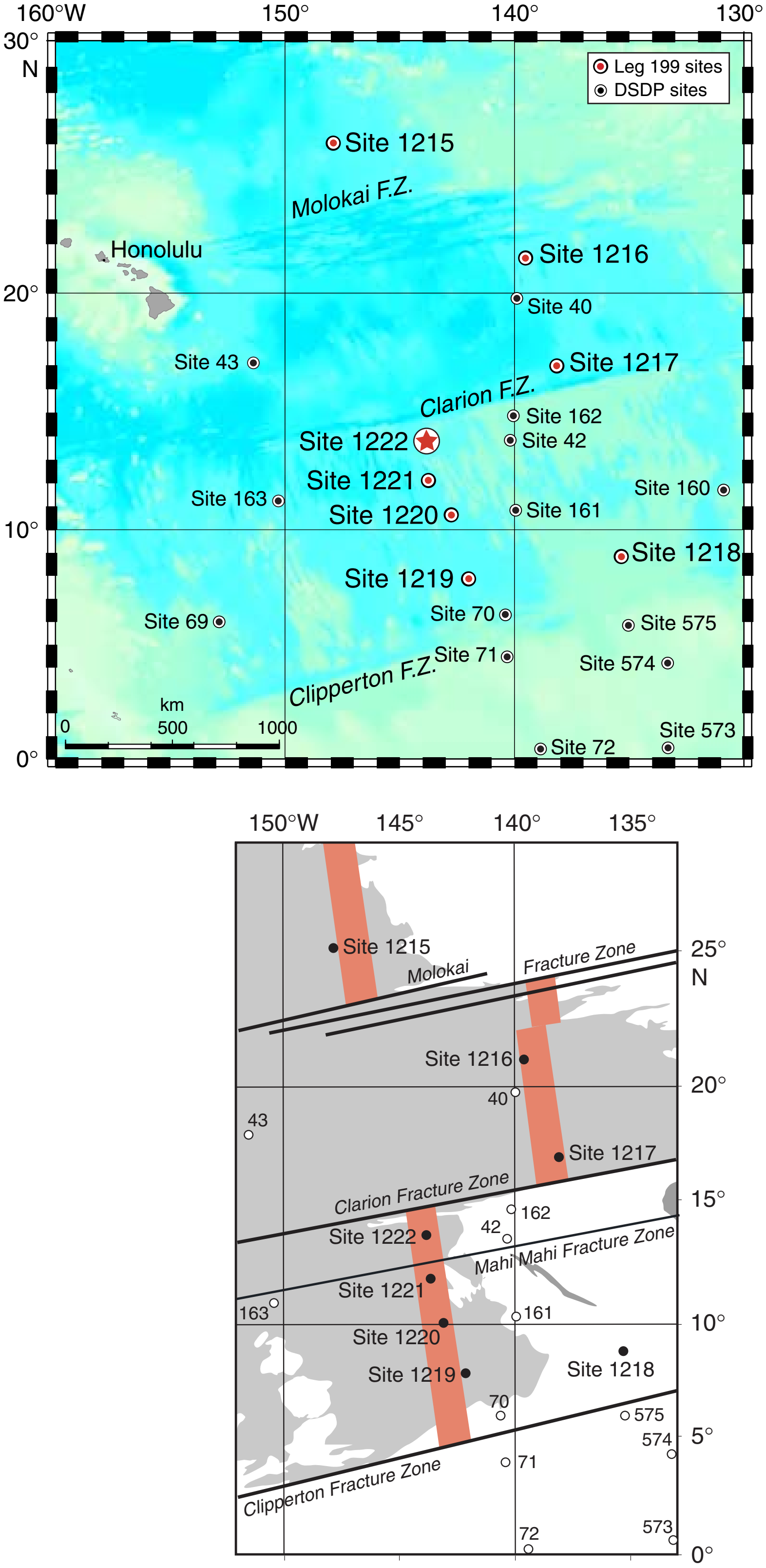

Figure F2. Seismic reflection profile through Site 1222. The sedimentary section is marked by a weakly reflective unit between the seafloor and ~62 ms two-way traveltime (TWT) below the seafloor, assumed to be clays. The next two prominent reflectors (~120 and 147 ms TWT mbsf) are interpreted to mark chert layers at the contact between middle and lower Eocene sediments and basement, respectively (see Lyle et al., this volume).

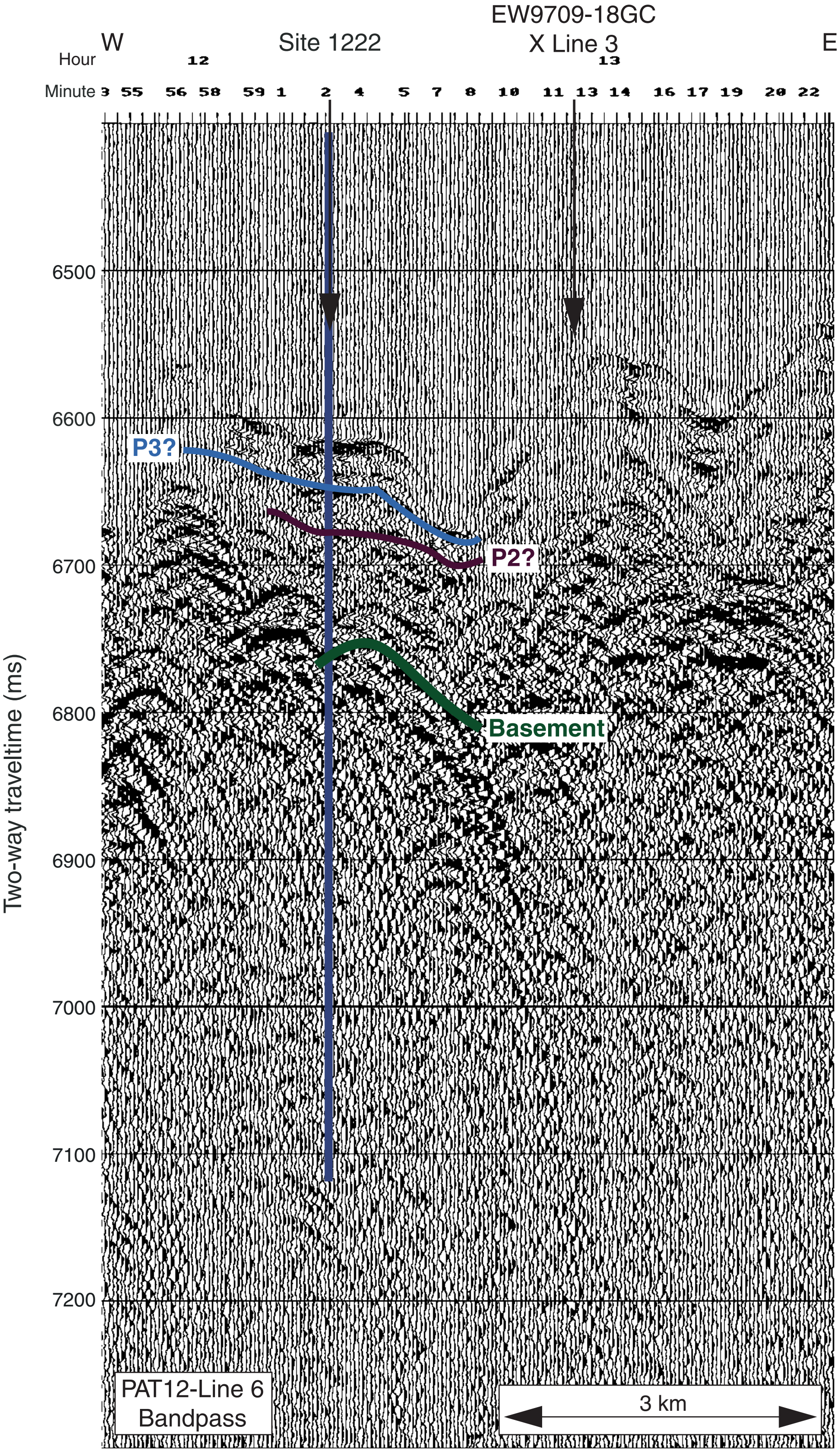

Figure F3. Lithologic summary for Site 1222. Note that lithologic units are based upon Hole 1222A recovery. LAS = light absorption spectroscopy, TD = total depth.

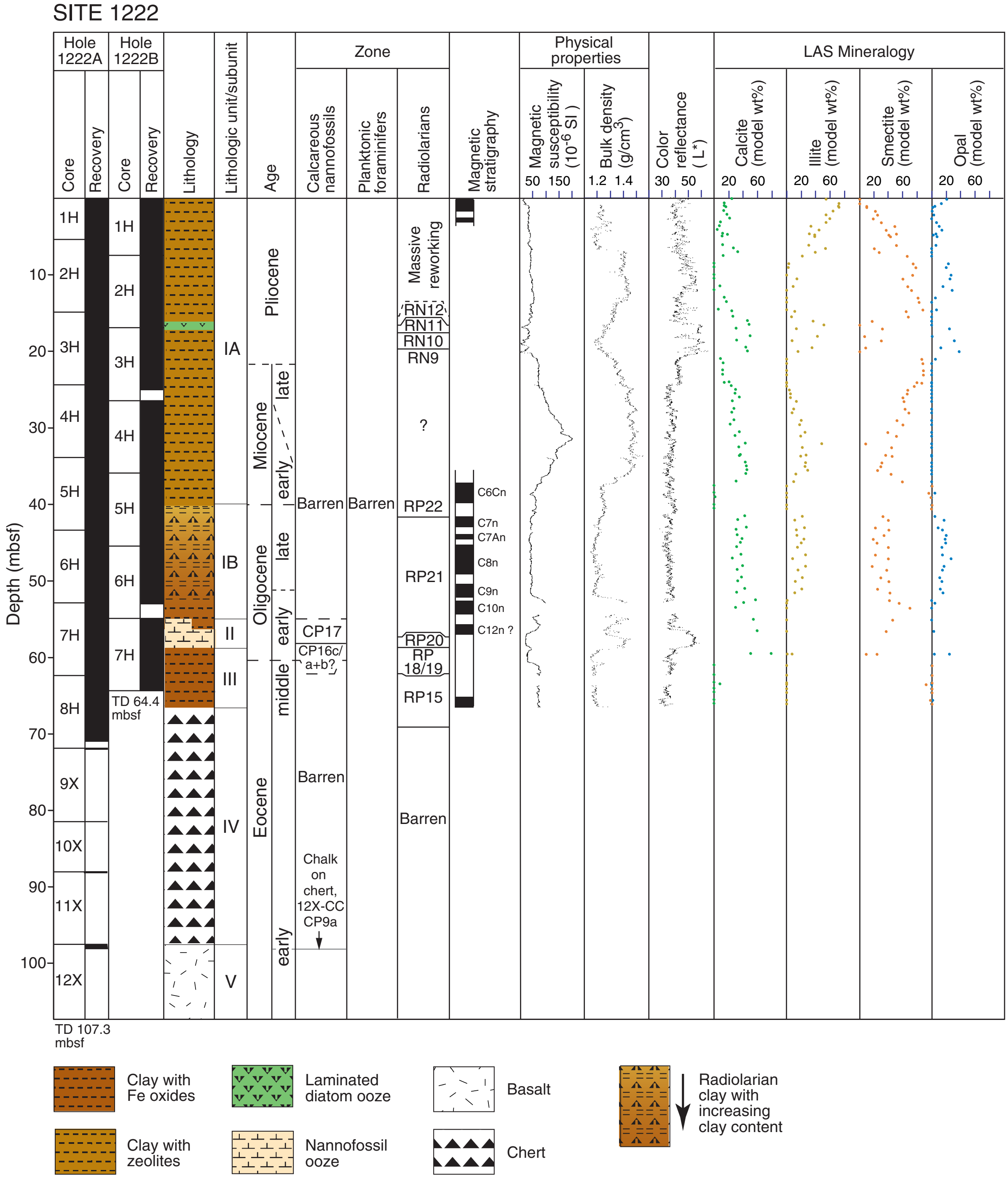

Figure F4. Close-up digital photograph of laminated diatom ooze (interval 199-1222A-3H-4, 50–100 cm; Unit I).

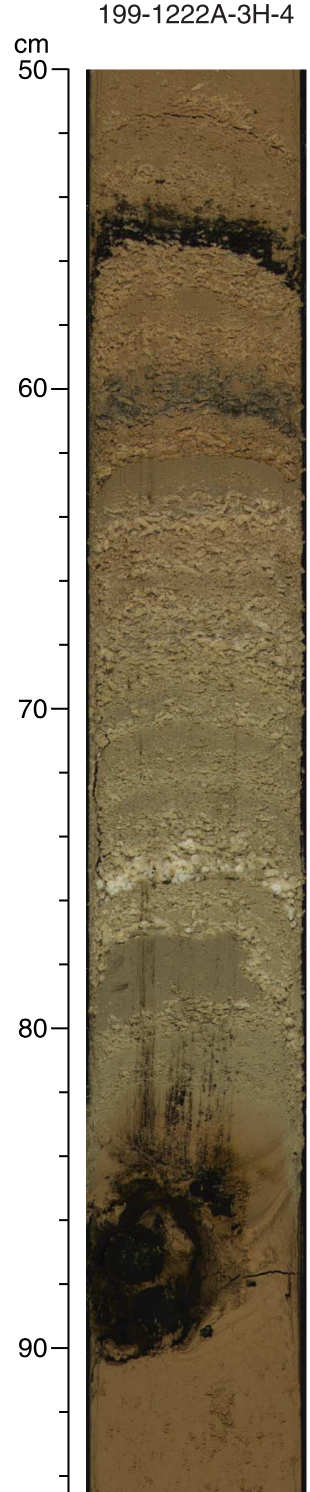

Figure F5. Calcareous and siliceous biostratigraphy for Site 1222. Horizontal dashed lines indicate that a boundary can only be approximated by available biostratigraphy. TD = total depth.

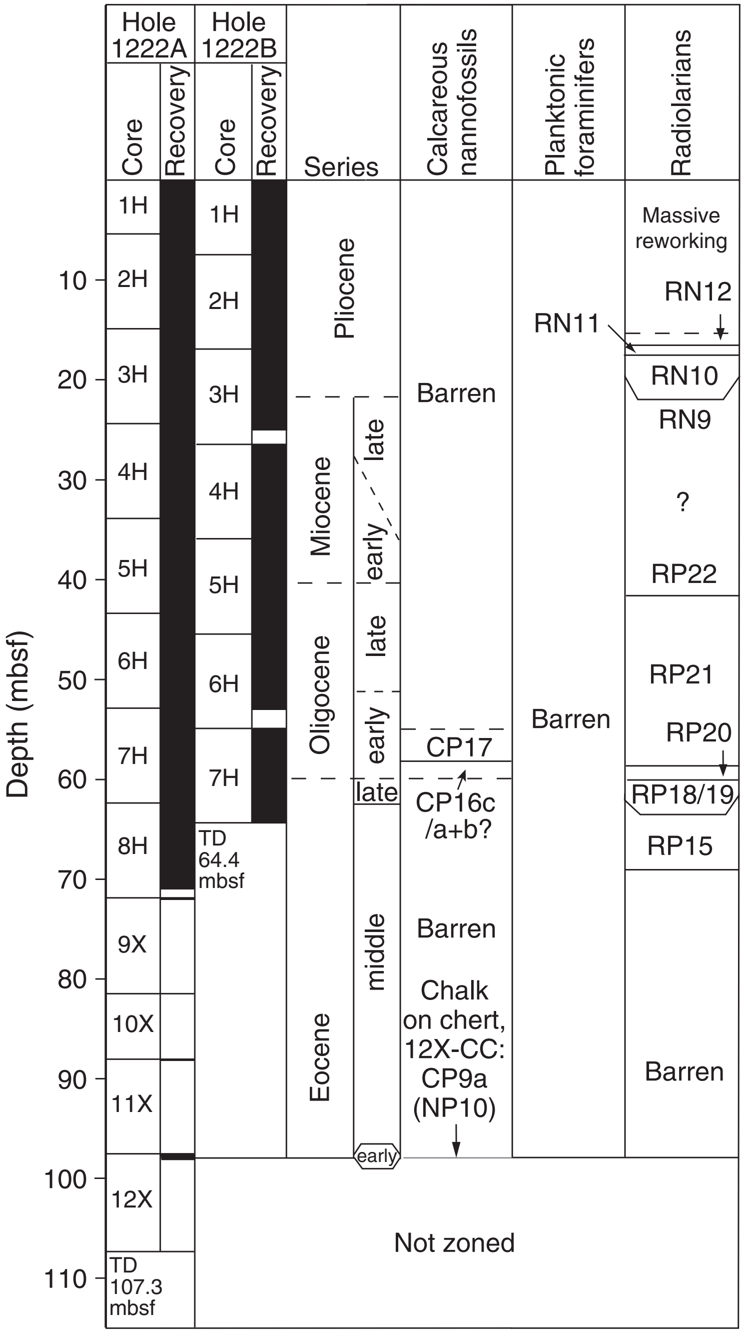

Figure F6. Archive-half magnetization intensities after AF demagnetization at a peak field of 20 mT for Holes 1222A and 1222B. Open circles = Hole 1222A, solid circles = Hole 1222B.

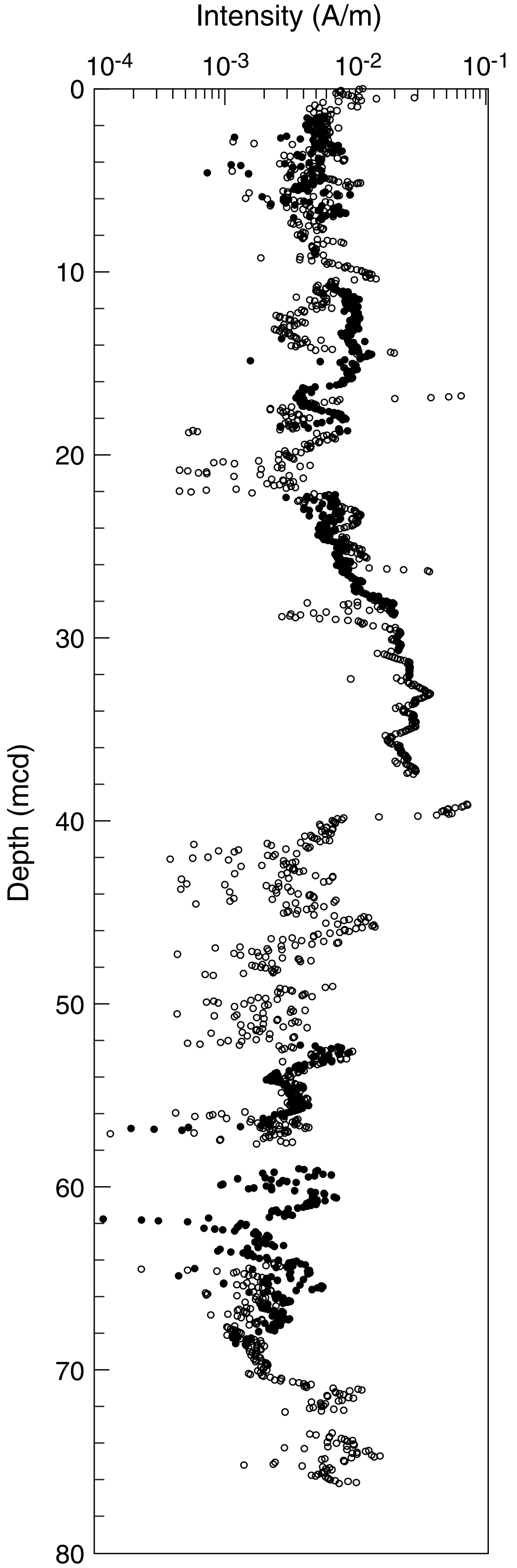

Figure F7. Composite magnetic stratigraphy at Site 1222. Virtual geomagnetic pole (VGP) latitudes were obtained after partial AF demagnetization of continuous measurements at a peak field of 20 mT. Polarity column shows interpreted zones of normal (black) and reversed (white) magnetization.

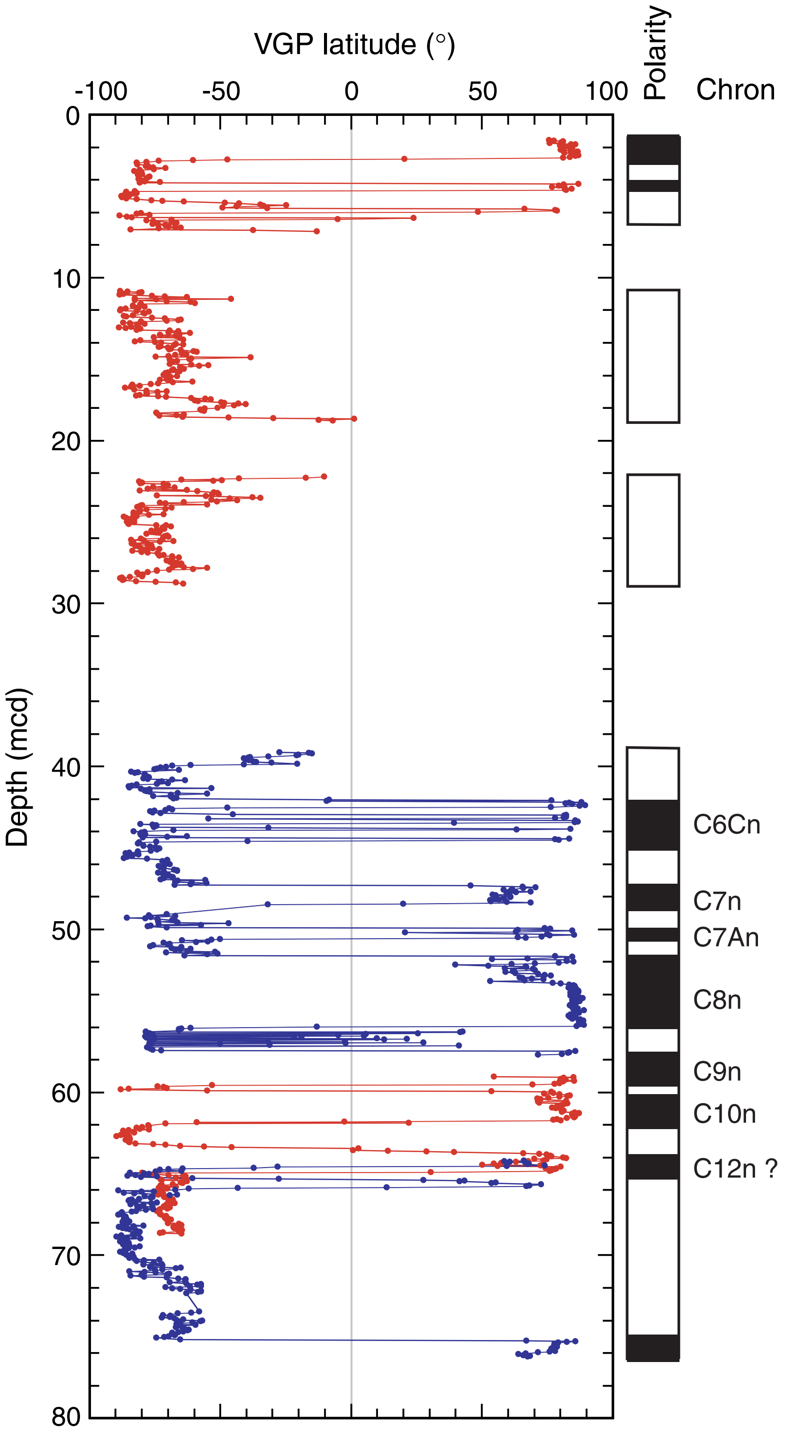

Figure F8. Gamma ray attenuation (GRA) bulk density, magnetic susceptibility, and color reflectance (L*) data for Holes 1222A (black; left curve in each panel) and 1222B (blue; right curve in each panel) plotted vs. composite depth. The data from Holes 1222B are offset by constants for illustration purposes. All data sets are smoothed with a nine-point Gaussian filter. Intervals with obvious flow-in or drilling disturbance are removed from the data sets (see Table T4, p. 45).

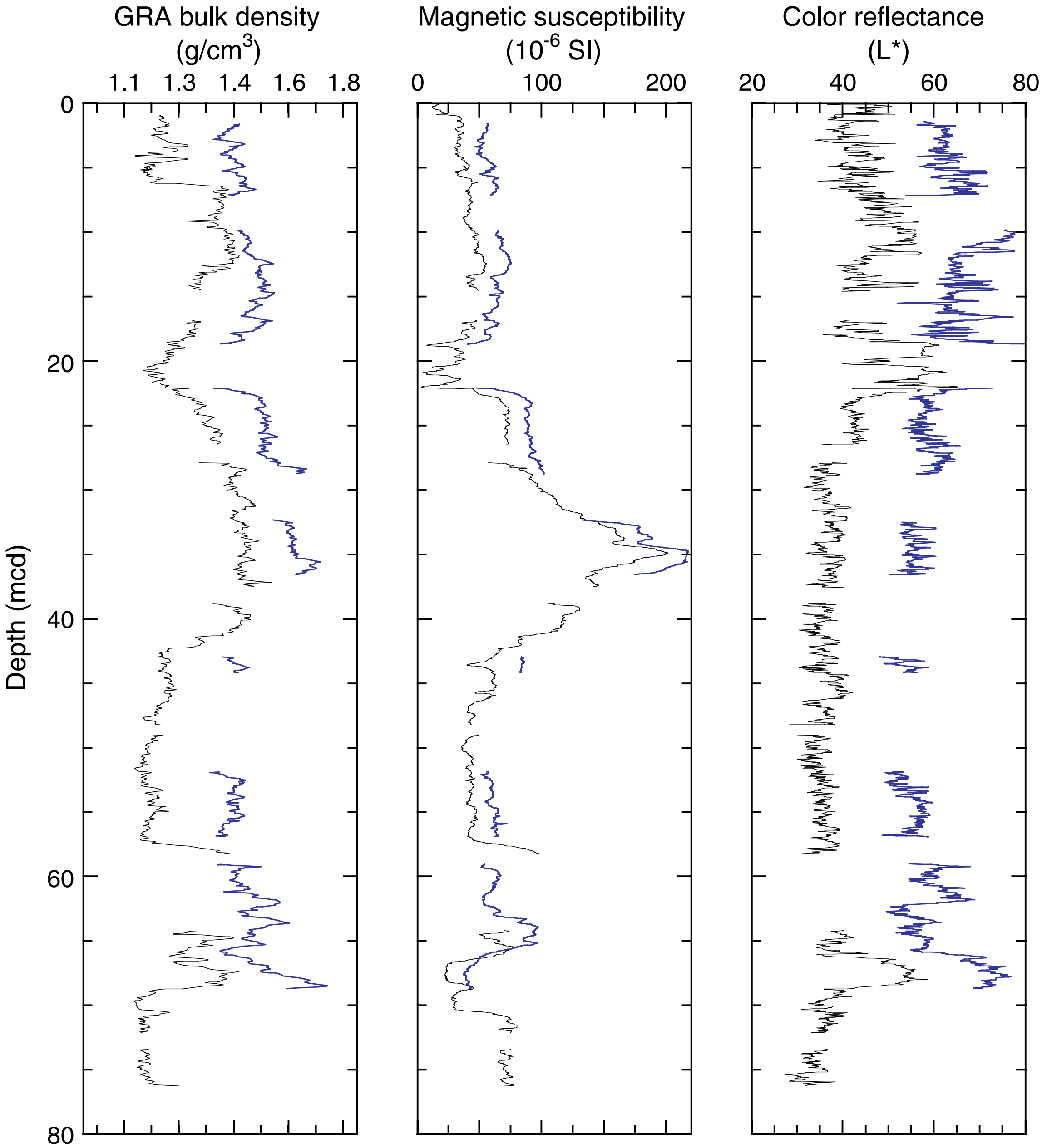

Figure F9. Spliced records of gamma ray attenuation (GRA) bulk density, magnetic susceptibility and the color reflectance parameter (L*) for Site 1222. Lithology changes are clearly visible just above ~70 mcd, where a more carbonate rich interval displays higher GRA bulk density and lower magnetic susceptibility values. The large jump in GRA bulk density observed at ~6 mcd is attributed to be an instrumental electronic artifact that was previously observed in Sites 1220 and 1221 GRA records.

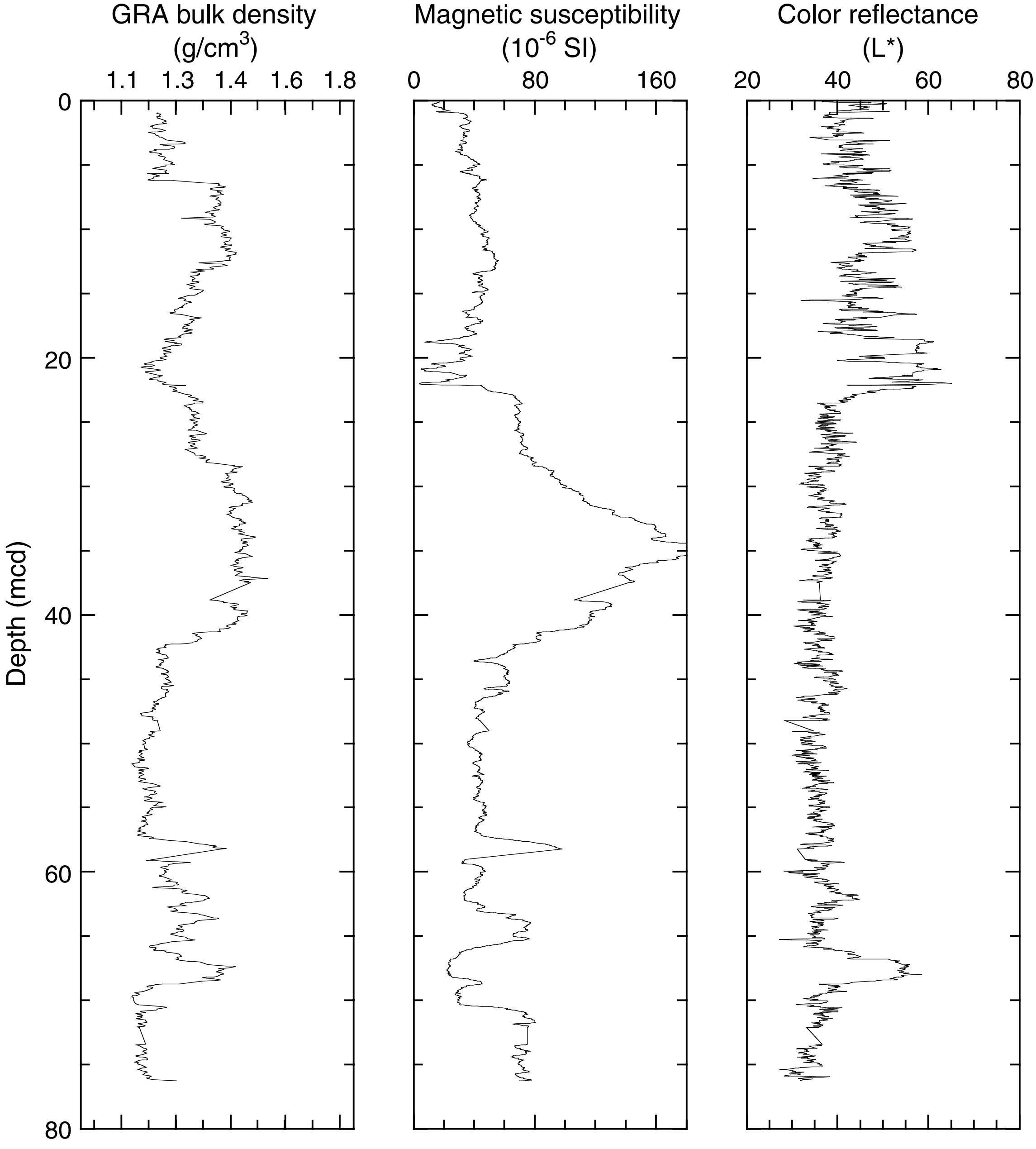

Figure F10. LSRs and chronostratigraphic markers for Site 1222.

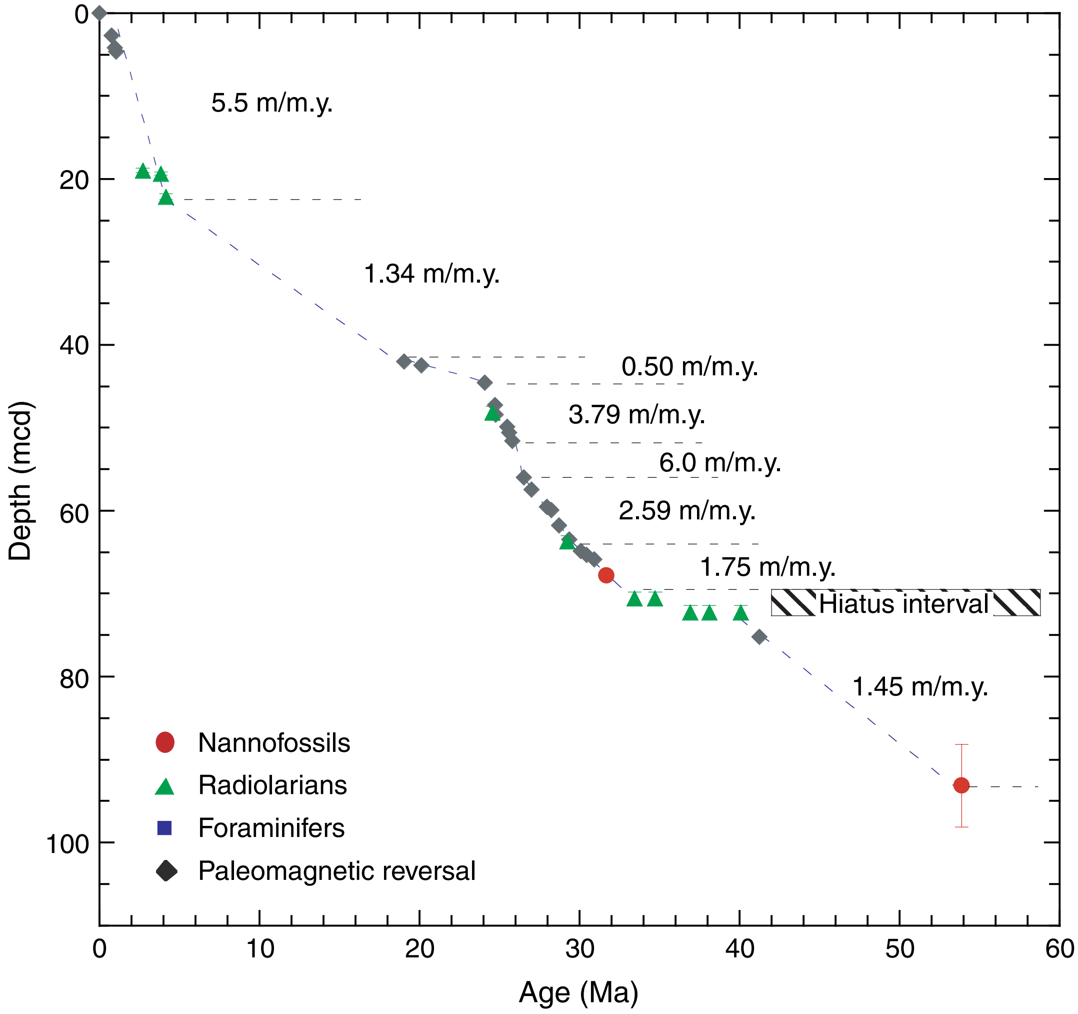

Figure F11. Density record of site survey piston Core EW9709-14P (red) compared to density record of Site 1222 (blue).

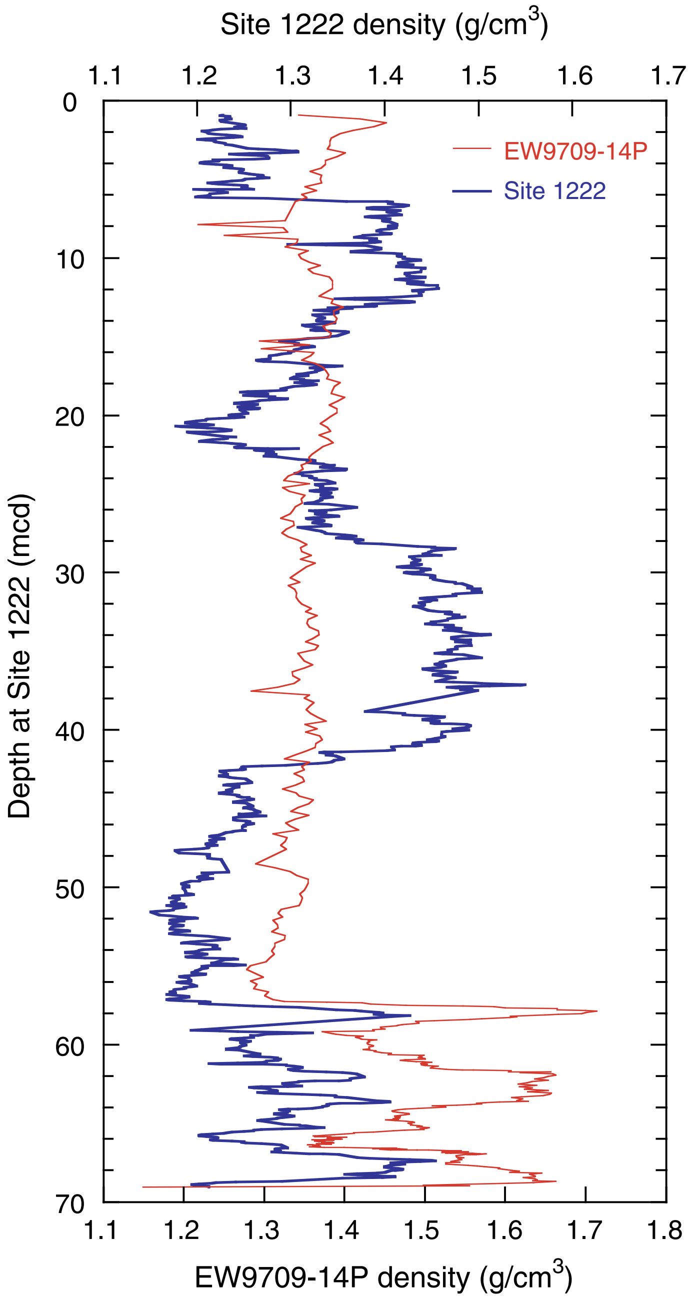

Figure F12. Mass accumulation rates (MARs) of sediments from Site 1222.

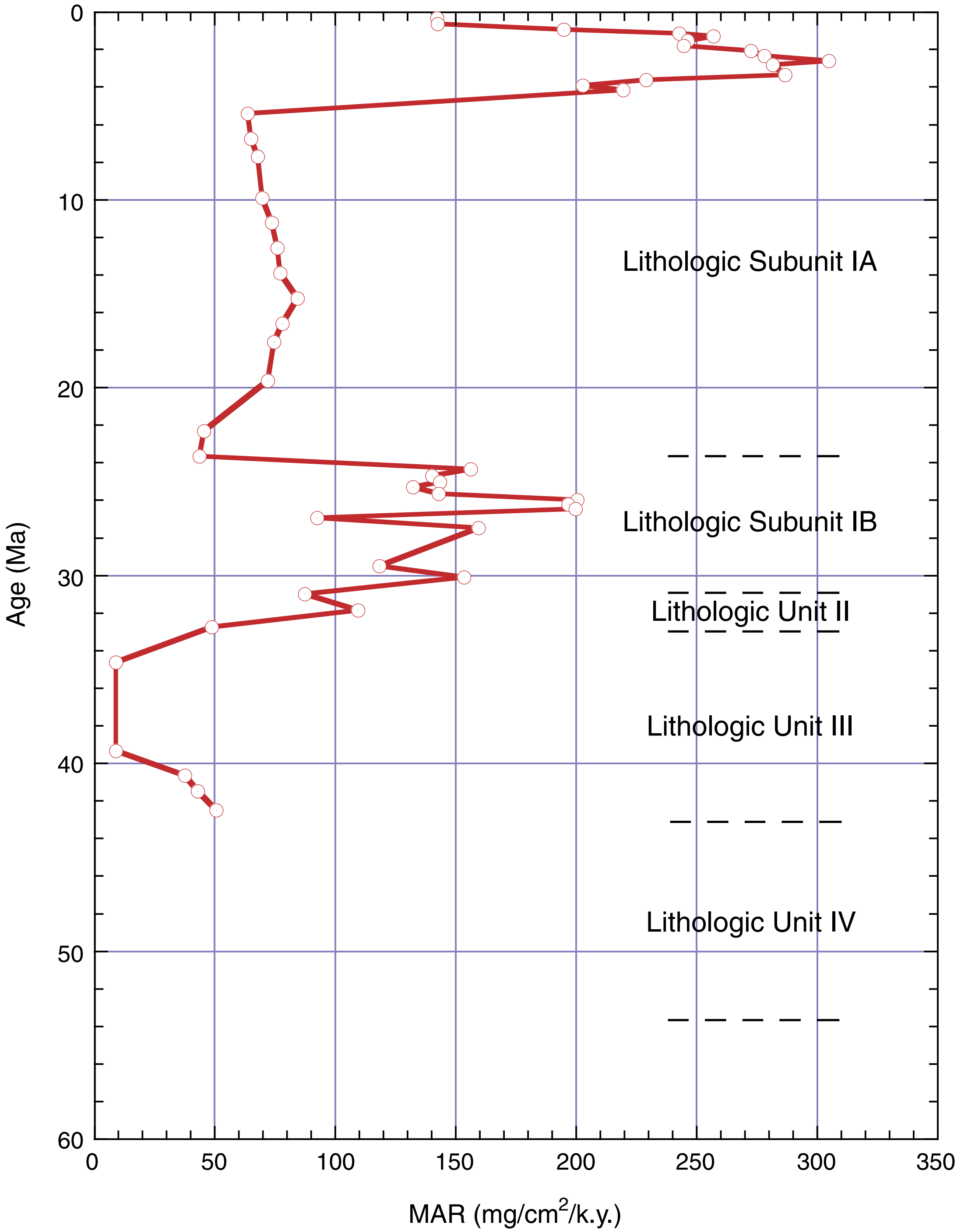

Figure F13. Interstitial water data from Site 1222. Solid circles = Ca, crosses = Mg.

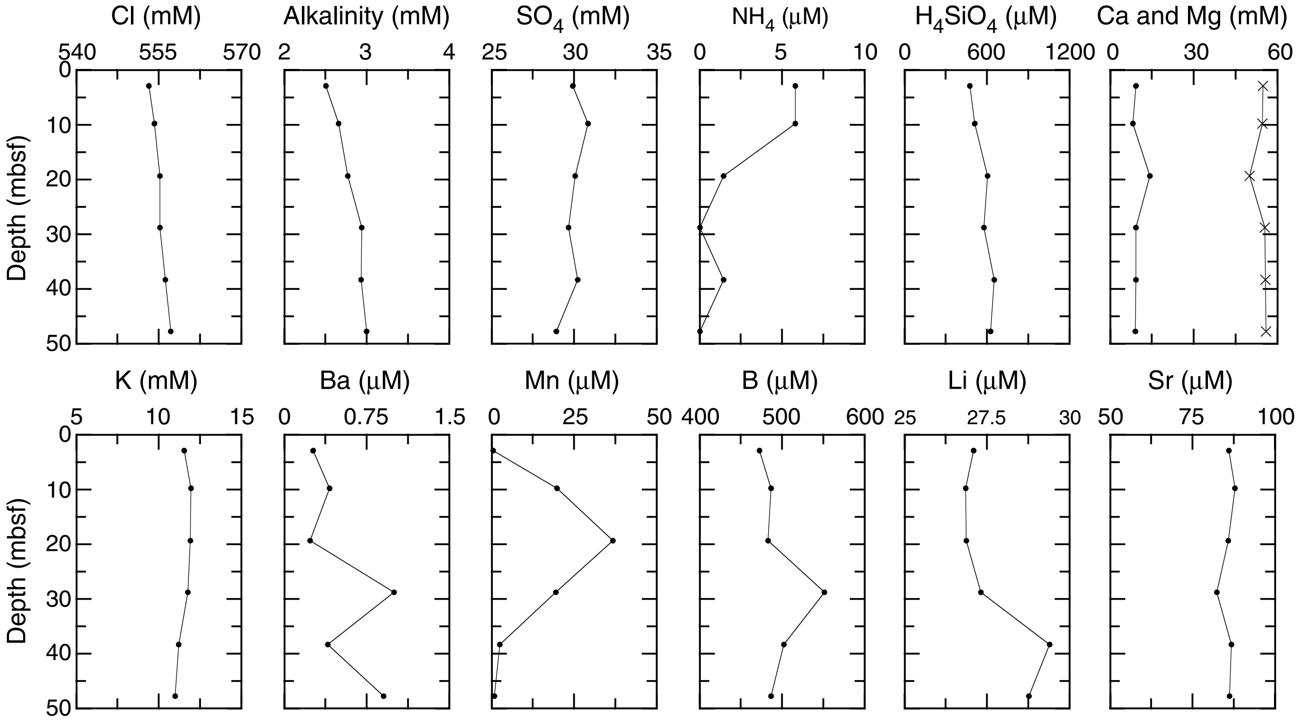

Figure F14. $CaCO_3$ data, determined by coulometric methods, from Site 1222.

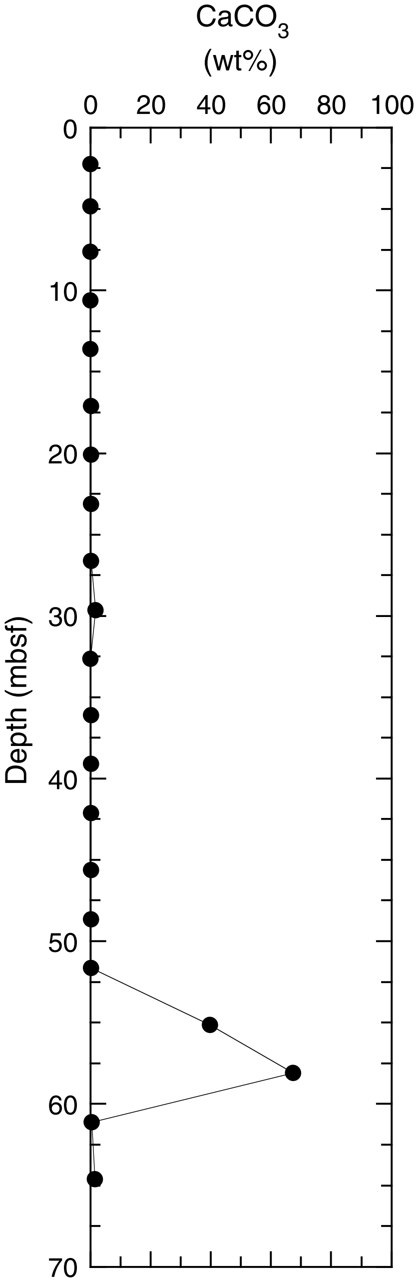

Figure F15. Moisture and density measurements for Hole 1222A. **A.** Porosity (solid symbols) and water content (open symbols). **B.** Discrete-sample wet bulk density (open symbols) and gamma ray attenuation (GRA) bulk density (line). **C.** Grain density. Lithologic Units I–V are noted on the right side of the figure.

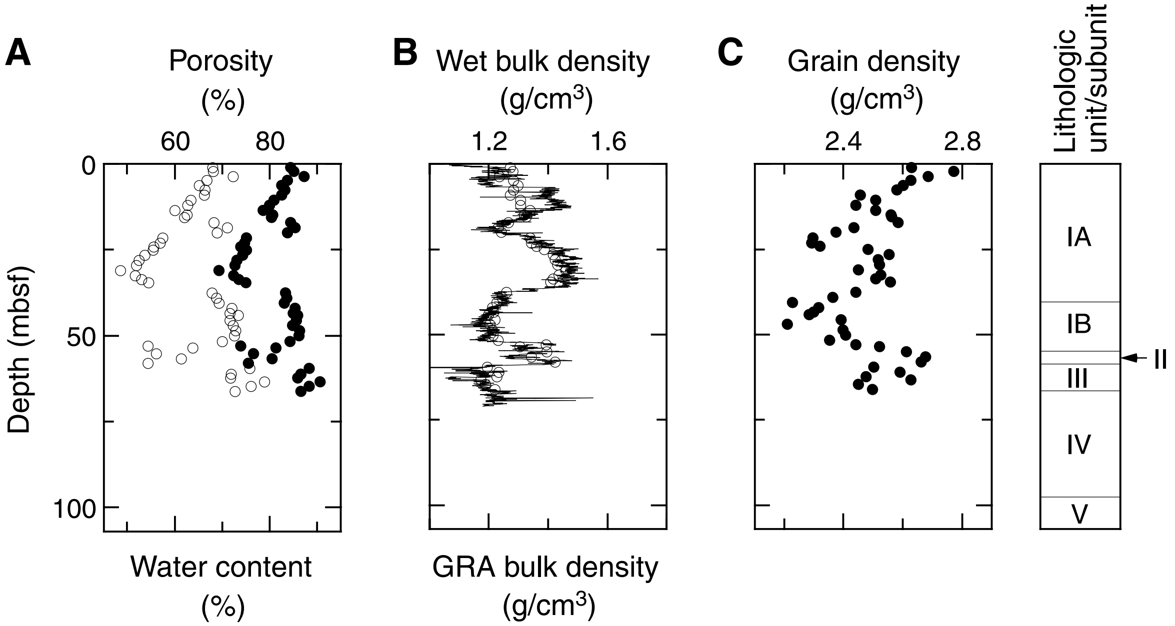

Figure F16. (**A**) Wet and (**B**) dry bulk density from discrete samples from Hole 1222A plotted with gamma ray attenuation (GRA) bulk density interpolated with a 20-cm-wide Gaussian window. GRA bulk densities from Sections 199-1222A-2H-2 through 2H-6, which appear to be offset by an electronic artifact in MST data acquisition, are not included in the comparison.

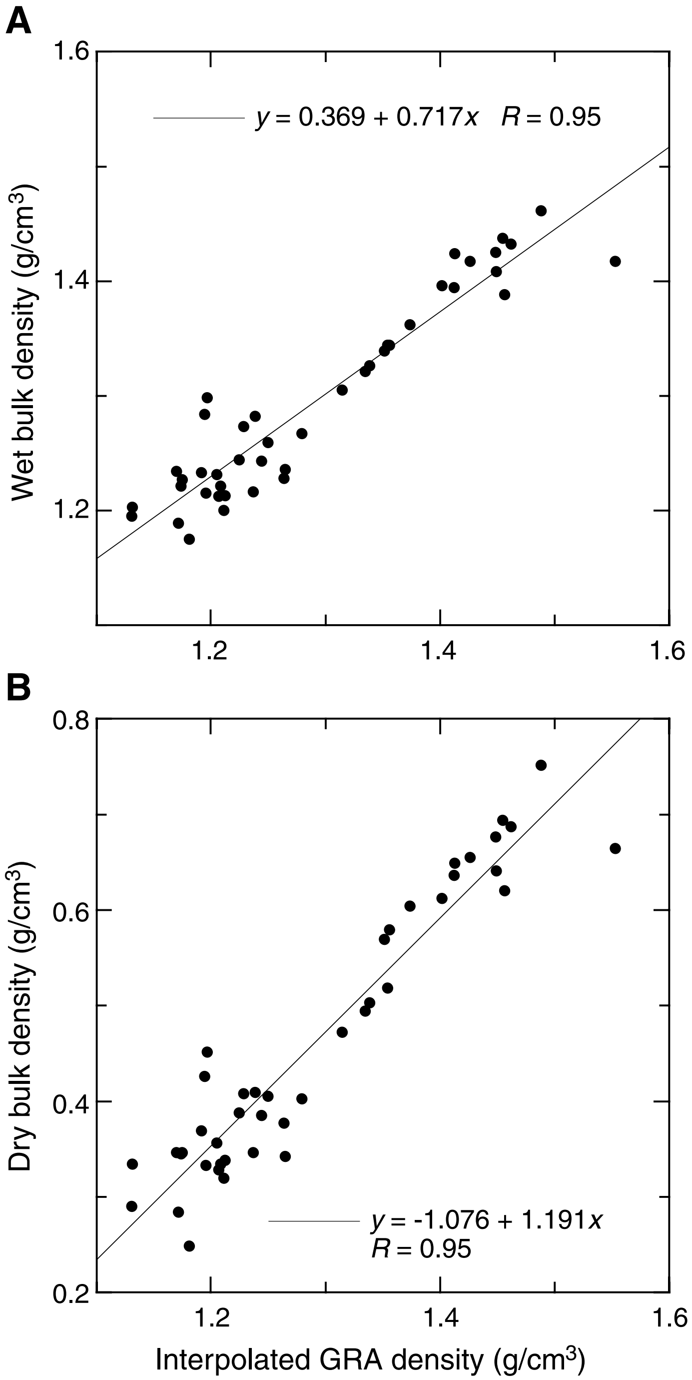

Figure F17. Comparison of magnetic susceptibility, gamma ray attenuation (GRA) bulk density, velocity, and natural gamma radiation with the digital core images from the diatom-rich Sections 199-1222A-3H-1 through 3H-5. cps = counts per second.

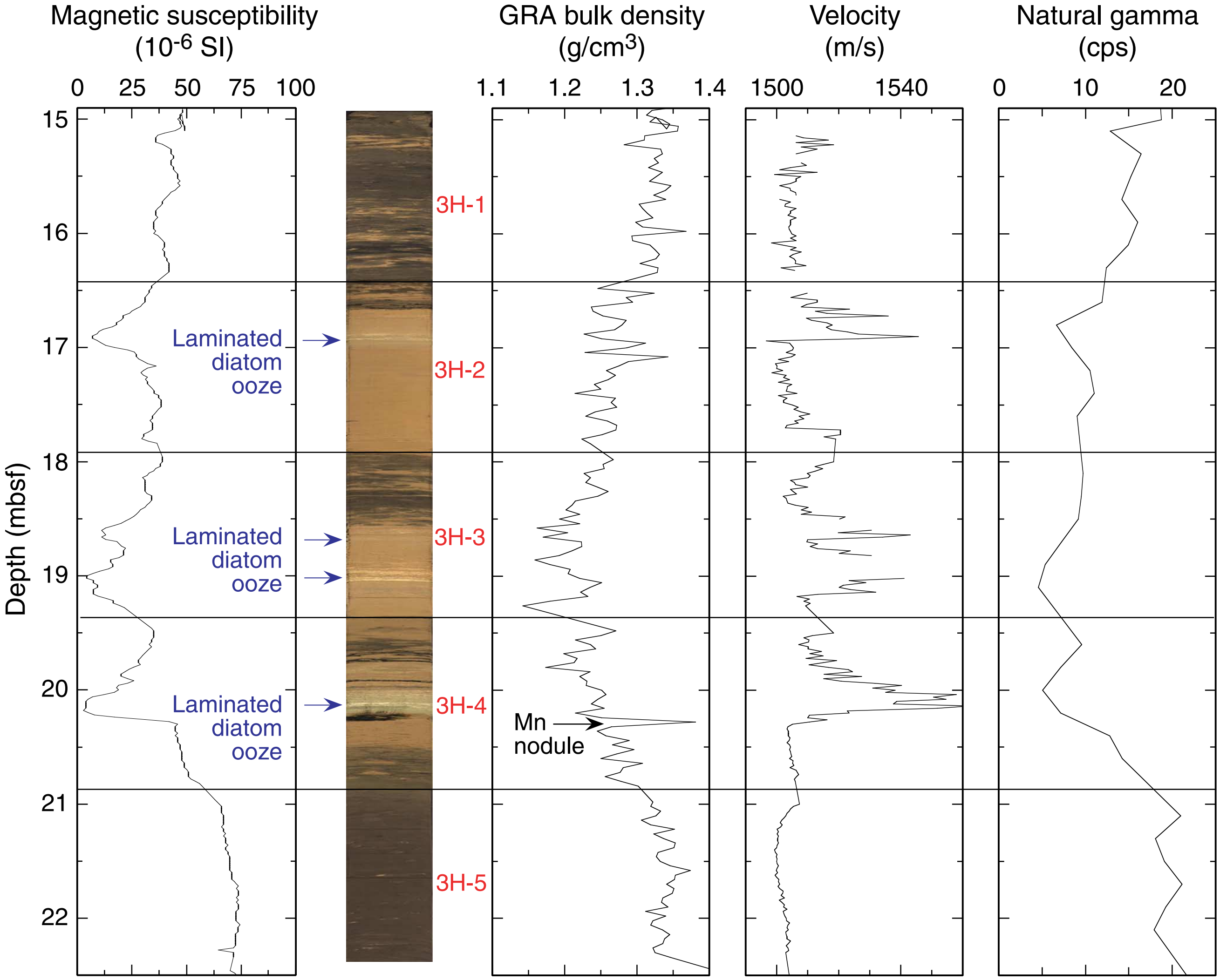

Figure F18. LAS mineralogy determinations for Hole 1222A. Lithologic Units I–III are noted to the left of the figure. Lam. diat. ooze = laminated diatom ooze.

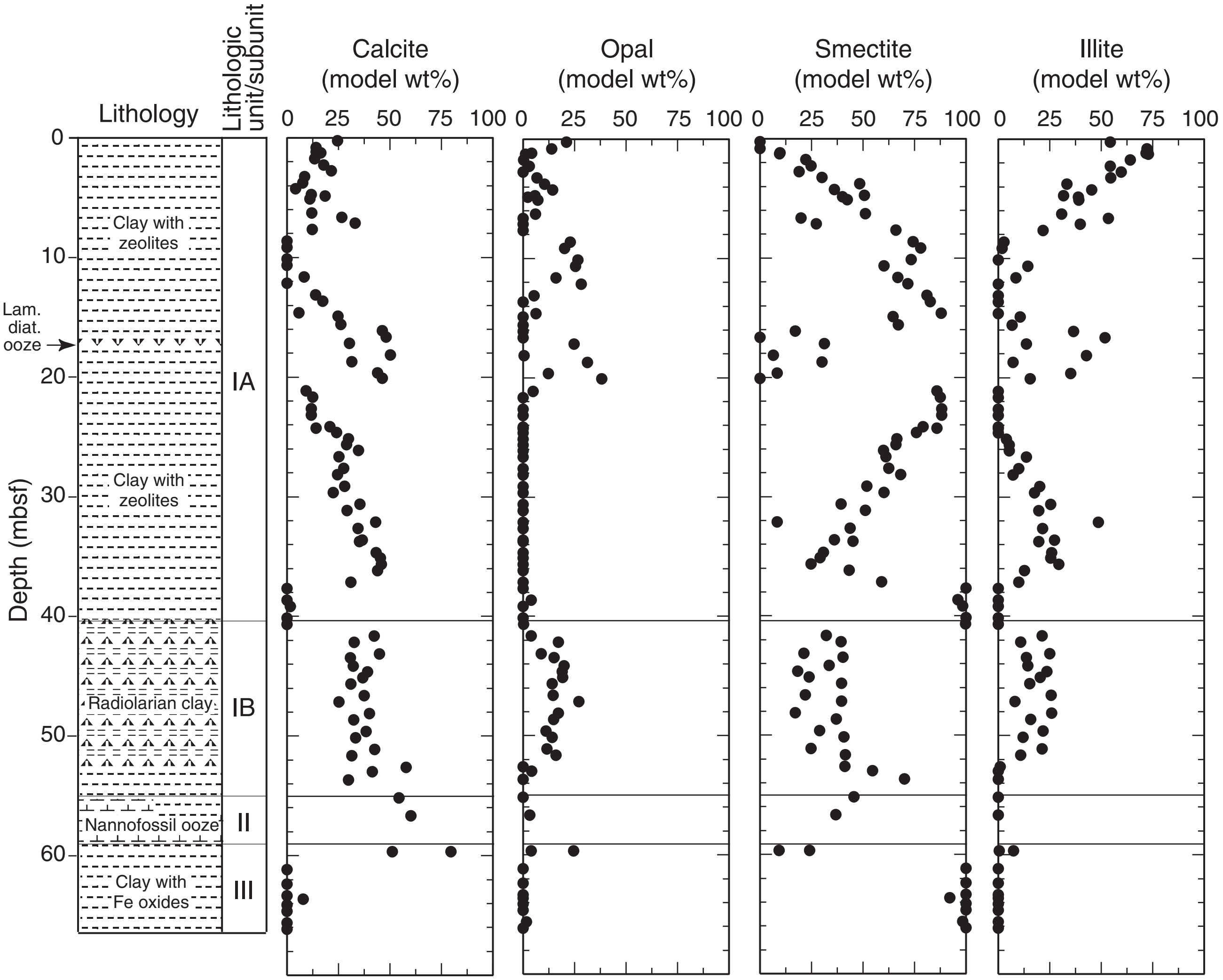

Figure F19. Compressional wave velocity from the PWL (line) and transverse velocity measured with the insertion (squares) and contact probe (circles) systems for Hole 1222A. Lithologic Units I–V are noted on the right side of the figure.

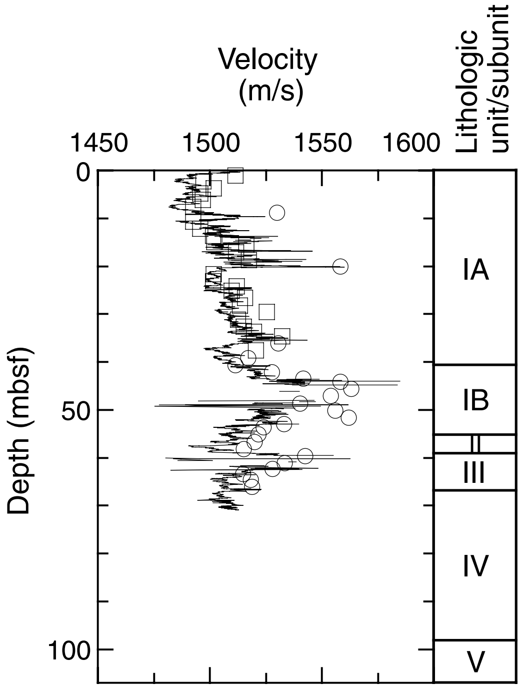

Figure F20. Thermal conductivity for Holes 1222A (solid symbols) and 1222B (open symbols). Lithologic Units I–V are noted on the right side of the figure.

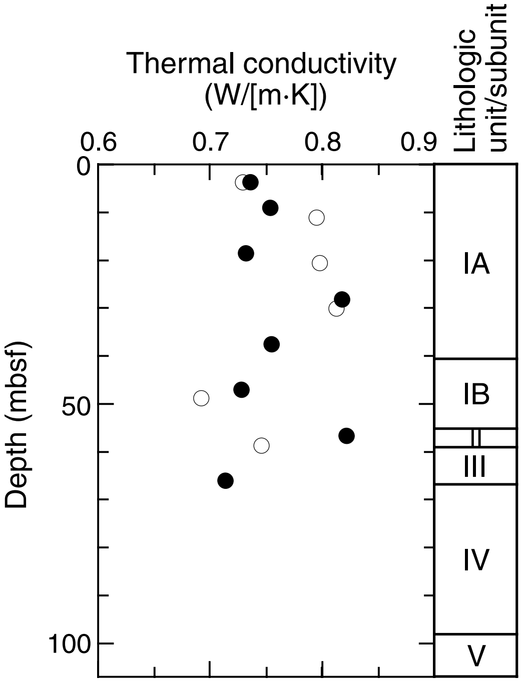

Figure F21. Natural gamma radiation for Hole 1222A. Lithologic Units I–V are noted on the right side of the figure. cps = counts per second.

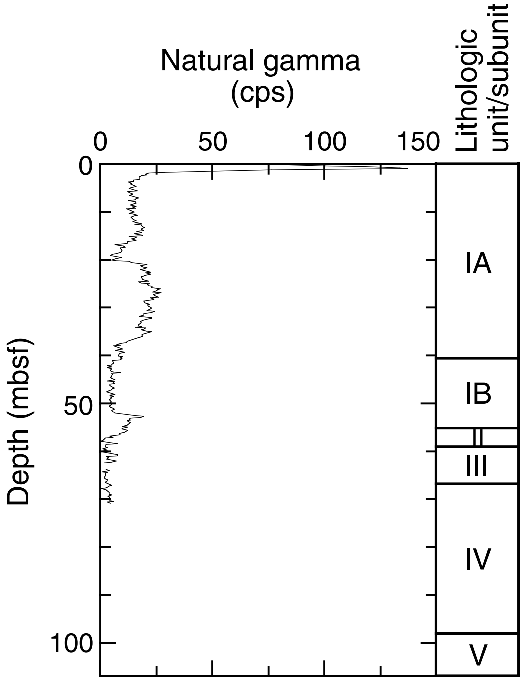

Figure F22. Magnetic susceptibility for Hole 1222A. Lithologic Units I–V are noted on the right side of the figure.

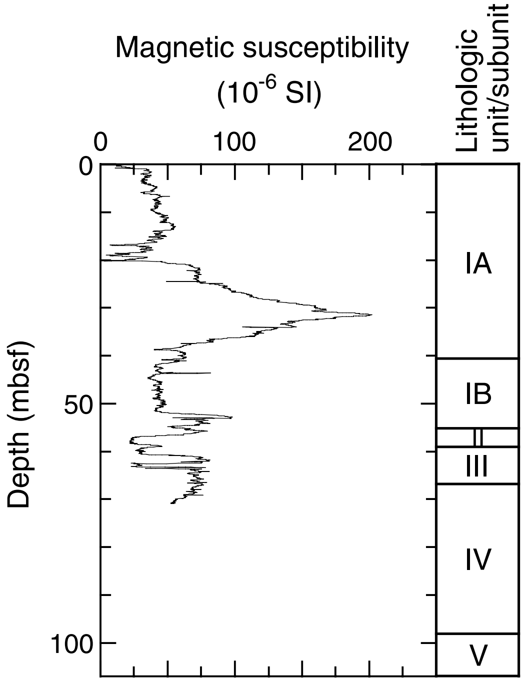

Table T1. Coring summary, Site 1222.

Hole 1222A

Latitude: 13°48.9780′N
Longitude: 143°53.3477′W
Time on site (hr): 57.75 (0745 hr, 10 Dec–1730 hr, 12 Dec 2001)
Time on hole (hr): 33.83 (0745 hr, 10 Dec–1735 hr, 11 Dec 2001)
Seafloor (drill pipe measurement from rig floor, mbrf): 5000.1
Distance between rig floor and sea level (m): 11.40
Water depth (drill pipe measurement from sea level, m): 4988.7
Total depth (drill pipe measurement from rig floor, mbrf): 5107.4
Total penetration (meters below seafloor, mbsf): 107.3
Total length of cored section (m): 107.3
Total core recovered (m): 74.64
Core recovery (%): 69.6
Total number of cores: 12
Total number of drilled intervals: 0

Hole 1222B

Latitude: 13°48.9776′N
Longitude: 143°53.3368′W
Time on hole (hr): 23.92 (1735 hr, 11 Dec–1730 hr, 12 Dec 2001)
Seafloor (drill pipe measurement from rig floor, mbrf): 5002.1
Distance between rig floor and sea level (m): 11.4
Water depth (drill pipe measurement from sea level, m): 4990.7
Total depth (drill pipe measurement from rig floor, mbrf): 5066.5
Total penetration (meters below seafloor, mbsf): 64.4
Total length of cored section (m): 64.4
Total core recovered (m): 63.77
Core recovery (%): 99.0
Total number of cores: 7
Total number of drilled intervals: 0

Core	Date (Dec 2001)	Local time (hr)	Depth (mbsf) Top	Depth (mbsf) Bottom	Length (m) Cored	Length (m) Recovered	Recovery (%)
199-1222A-							
1H	10	1845	0.0	5.4	5.4	5.40	100.0
2H	10	2000	5.4	14.9	9.5	9.93	104.5
3H	10	2110	14.9	24.4	9.5	9.92	104.4
4H	10	2220	24.4	33.9	9.5	10.04	105.7
5H	10	2340	33.9	43.4	9.5	10.04	105.7
6H	11	0055	43.4	52.9	9.5	10.08	106.1
7H	11	0205	52.9	62.4	9.5	9.87	103.9
8H	11	0430	62.4	71.9	9.5	8.73	91.9
9X	11	0810	71.9	81.5	9.6	0.09	0.9
10X	11	1040	81.5	88.1	6.6	0.01	0.2
11X	11	1315	88.1	97.7	9.6	0.08	0.8
12X	11	1630	97.7	107.3	9.6	0.45	4.7
				Cored totals:	107.3	74.64	69.6
199-1222B-							
1H	11	1940	0.0	7.4	7.4	7.38	99.7
2H	11	2050	7.4	16.9	9.5	9.77	102.8
3H	11	2210	16.9	26.4	9.5	9.19	96.7
4H	12	0130	26.4	35.9	9.5	9.76	102.7
5H	12	0255	35.9	45.4	9.5	9.95	104.7
6H	12	0415	45.4	54.9	9.5	7.73	81.4
7H	12	0545	54.9	64.4	9.5	9.99	105.2
				Cored totals:	64.4	63.77	99.0

Note: The expanded coring summary table is available in ASCII (see the **"Supplementary Material"** contents list).

Table T2. Summary of radiolarian zonal boundary ages calibrated using the paleomagnetic reversals, Hole 1220A. (See table notes. Continued on next two pages.)

Core, section, interval (cm)	Depth		Preservation	Abundance	Zone	*Anthocyrtidium angulare*	*Artophormis gracilis*	*Calocyclas bandyca*	*Calocyclas hispida*	*Calocyclas turris*	*Calocycletta robusta*	*Centrobotrys gravida*	*Cryptocarpium azyx*	*Dictyoprora mongolfieri*	*Didymocyrtis penultima*	*Didymocyrtis tetrathalamus*	*Dorcadospyris ateuchus*	*Dorcadospyris circulus*	*Dorcadospyris forcipata*	*Dorcadospyris papilio*	*Dorcadospyris pseudopapilio*	*Dorcadospyris quadripes*	*Dorcadospyris spinosa*	*Eucyrtidium diaphanes*	*Eusyringium fistuligerum*	*Eusyringium lagena*	*Lamprocyrtis daniellae*	*Lamprocyrtis heteroporos*	*Lamprocyrtis neoheteroporos*	*Lamprocyrtis nigriniae*	*Lithochytris vespertilio*	*Lithocyclia aristotelis*	*Lithocyclia crux*	*Lithocyclia ocellus* gp.	*Lophocyrtis jacchia*	*Lychnocanoma bellum*	*Lychnocanoma elongata*	*Lychnodictyum audax*	*Phormocyrtis striata striata*	*Phormostichoartus doliolum*	*Phormostichoartus fistula*	*Podocyrtis (Lampterium) chalara*	*Podocyrtis (Lampterium) goetheana*	*Podocyrtis (Lampterium) mitra*	*Podocyrtis (Lampterium) trachodes*
	(mbsf)	(mcd)																																											
199-1222A-																																													
1H-CC	5.37	5.37	M	F	?				(P)				(P)	(P)								(P)			(P)	(P)						(P)		(P)					(P)			(P)	(P)	(P)	(P)
2H-CC	15.30	14.74	M	F	?			(P)	(P)	(P)			(P)																					(P)								(P)	(P)		
3H-2, 14–16	16.54	18.42			RN12	+																							P	P															
3H-2, 110–112	17.50	19.38			RN10																						P	P												P					
3H-3, 42–44	18.32	20.20			RN10																								P																
3H-4, 18–20	19.58	21.46	G	C	RN10?	+									P	P													?									P			P				
3H-4, 88–90	20.28	22.16	M	C	RN9										P																														
3H-CC	24.78	26.66	P	R	?																																								
4H-CC	34.40	37.84		T	?																																								
5H-3, 45–47	37.35	42.23																																											
5H-4, 45–47	38.85	43.73		B	?																																								
5H-5, 45–47	40.35	45.23																																											
5H-6, 45–47	41.85	46.73		F/C	RP22						P						P		P	P																	P								
5H-7, 45–47	43.35	48.23		P/M																																									
5H-CC	43.90	48.78	M	C	RP21				(P)		P			(P)			P	—	P	P					(P)												—								
6H-1, 45–47	43.85	49.19																																											
6H-2, 45–47	45.35	50.69																																											
6H-3, 45–47	46.85	52.19																																											
6H-4, 45–47	48.35	53.69																																											
6H-5, 45–47	49.85	55.19																																											
6H-6, 45–47	51.35	56.69																																											
6H-CC	53.45	58.79		T	?												+																												
7H-2, 45–47	54.85	64.58	P	R																																									
7H-3, 45–47	56.35	66.08	P	R	?																																								
7H-4, 45–47	57.85	67.58	M/P	C	RP20																	P	P		(P)																				
7H-5, 45–47	59.35	69.08	M	C	RP20		P	P	P	P		P	(P)	P							P	P			P	(P)						P		P									P		(P)
7H-6, 45–47	60.85	70.58	P	R	RP18?		P							P											P						P			P	P				P				P		
7H-7, 66–68	62.56	72.29	G	A	RP15				P					P											P						P			P								P		P	
7H-CC	62.72	72.45			RP15				P																P						P			P								P		+	
8H-2, 45–47	64.35	74.08	P	R	RP15									P																												P			
8H-3, 45–47	65.85	75.58	P	R	RP15																																					P			
8H-CC	71.08	80.81		T	?																																								
10X-CC	81.50	81.50		B																																									
12X-CC	97.70	97.70																																											

Table T2 (continued).

Core, section, interval (cm)	Depth (mbsf)	Depth (mcd)	Preservation	Abundance	Zone	*Podocyrtis (Podocyrtis) papalis*	*Podocyrtis (Podocyrtoges) ampla*	*Pterocanium prismatium*	*Sethochytris triconiscus*	*Spongaster pentas*	*Spongaster tetras tetras*	*Spongatractus pachystylus*	*Stichocorys peregrina*	*Theocorythium trachelium trachelium*	*Theocorythium vetulum*	*Theocorys anaclasta*	*Theocotyle venezuelensis*	*Theocotylissa ficus*	*Theocyrtis annosa*	*Theocyrtis tuberosa*	*Thyrsocyrtis (Pentalacorys) lochites*	*Thyrsocyrtis (Pentalacorys) tetracantha*	*Thyrsocyrtis (Pentalacorys) triacantha*	*Thyrsocyrtis (Thyrsocyrtis) bromia*	*Thyrsocyrtis (Thyrsocyrtis) rhizodon*	*Thyrsocyrtis (Thyrsocyrtis) robusta*	*Tristylospyris triceros*
199-1222A-																											
1H-CC	5.37	5.37	M	F	?									P		(P)							(P)		(P)	(P)	
2H-CC	15.30	14.74	M	F	?		(P)		(P)			(P)								(P)	(P)		(P)				
3H-2, 14–16	16.54	18.42			RN12			P			?		P														
3H-2, 110–112	17.50	19.38			RN10			P					P		P												
3H-3, 42–44	18.32	20.20			RN10			P		P			P		P												
3H-4, 18–20	19.58	21.46	G	C	RN10?			P					P		P												
3H-4, 88–90	20.28	22.16	M	C	RN9								P		P												
3H-CC	24.78	26.66	P	R	?																						
4H-CC	34.40	37.84		T	?																						
5H-3, 45–47	37.35	42.23																									
5H-4, 45–47	38.85	43.73		B	?																						
5H-5, 45–47	40.35	45.23																									
5H-6, 45–47	41.85	46.73		F/C	RP22																						
5H-7, 45–47	43.35	48.23		P/M																							
5H-CC	43.90	48.78	M	C	RP21	(P)						(P)							P			(P)	(P)				
6H-1, 45–47	43.85	49.19																									
6H-2, 45–47	45.35	50.69																									
6H-3, 45–47	46.85	52.19																									
6H-4, 45–47	48.35	53.69																									
6H-5, 45–47	49.85	55.19																									
6H-6, 45–47	51.35	56.69																									
6H-CC	53.45	58.79		T	?																		(P)				
7H-2, 45–47	54.85	64.58	P	R																			P				P
7H-3, 45–47	56.35	66.08	P	R	?																						
7H-4, 45–47	57.85	67.58	M/P	C	RP20															P							(P)
7H-5, 45–47	59.35	69.08	M	C	RP20		(P)					P					(P)			P			P	P	P		P
7H-6, 45–47	60.85	70.58	P	R	RP18?																	P	P		P		P
7H-7, 66–68	62.56	72.29	G	A	RP15	P			P			P											P				P
7H-CC	62.72	72.45			RP15	P			P			P										P	P		P		P
8H-2, 45–47	64.35	74.08	P	R	RP15																		P		P		
8H-3, 45–47	65.85	75.58	P	R	RP15																		P				
8H-CC	71.08	80.81		T	?																						
10X-CC	81.50	81.50		B																							
12X-CC	97.70	97.70																									

Table T2 (continued).

Notes: Preservation: G = good, M = moderate, P = poor. Abundance: A = abundant, C = common, F = few, R = rare, T = trace, P = present, (P) = present, reworked, + = very rare, — = absent. Magnetostratigraphically-derived ages for the boundaries between Zones RN12 and RN11, between RN11 and RN10, and between RN10 and RN9 are already well established (Shackleton et al., 1995), and the magnetics at Site 1222 do not suggest any changes to those ages. An age of 24.6 Ma was determined by Sanfilippo and Nigrini (1996) for the RP21/RP20 zonal boundary and is not changed herein. Subsequent assumed downhole ages for zonal boundaries are approximations (Sanfilippo and Nigrini, 1998). The ages calculated from the geomagnetic reversals in Site 1220 are generally somewhat older than the Sanfilippo and Nigrini (1998) ages.

Table T3. Radiolarian zonal boundaries, Site 1222.

Zonal boundaries	Age (Ma)	Hole, core, section, interval (cm)		Depth (mbsf)		Depth (mcd)	
		Top	Bottom	Midpoint	±	Midpoint	±
		199-	199-				
RN12/11	2.74	1222A-3H-2, 14	1222B-2H-CC	16.84	0.30	18.71	0.29
RN11/10	3.87	1222B-2H-CC	1222A-3H-2, 110	17.32	0.18	19.19	0.19
RN10/9	4.19	1222A-3H-4, 18	1222A-3H-4, 88	19.93	0.35	21.81	0.35
RP22/21	24.60	1222A-5H-6, 45	1222A-5H-7, 45	42.60	0.75	47.48	0.75
RP21/20	29.27	1222B-7H-3, 45	1222B-7H-4, 19	58.98	0.63	63.07	0.63
RP20/19	33.47	1222A-7H-5, 45	1222A-7H-6, 45	60.10	0.75	69.83	0.75
RP19/18	34.77	1222A-7H-5, 45	1222A-7H-6, 45	60.10	0.75	69.83	0.75
RP18/17	36.96	1222A-7H-6, 45	1222A-7H-7, 66	61.71	0.86	71.44	0.86
RP17/16	38.12	1222A-7H-6, 45	1222A-7H-7, 66	61.71	0.86	71.44	0.86
RP16/15	40.12	1222A-7H-6, 45	1222A-7H-7, 66	61.71	0.86	71.44	0.86

Notes: * = new ages calibrated from paleomagnetic reversals at Site 1220. This table is also available in **ASCII.**

Table T4. Core disturbance, Site 1222.

Core, section, interval (cm)	Depth (mbsf)		Comments
	Top	Bottom	
199-1222A-			
1H-1, 0–1	0.00	0.01	Soupy
4H-1, 0–7	24.40	24.47	Soupy
6H-1, 0–31	43.40	43.71	Disturbed (slightly)
7H-1, 0–10	52.90	53.00	Soupy
7H-1, 10–150	53.00	54.40	Disturbed (slightly)
8H-1, 0–80	62.40	63.20	Soupy
8H-1, 80–130	63.20	63.70	Flow-in
8H-3, 115–150	66.55	66.90	Flow-in
8H-4, 0–150	66.90	68.40	Flow-in
8H-5, 0–150	68.40	69.90	Flow-in
8H-6, 0–111	69.90	71.01	Flow-in
199-1222B-			
1H-1, 0–140	0.00	1.40	Flow-in
2H-1, 0–30	7.40	7.70	Soupy
2H-1, 30–60	7.70	8.00	Disturbed
2H-4, 112–118	13.02	13.08	Void
2H-6, 8–10	14.96	14.98	Void
2H-6, 119–120	16.07	16.08	Void
3H-1, 0–150	16.90	18.40	Soupy
3H-2, 0–14	18.40	18.54	Soupy
3H-2, 4–85	18.44	19.25	Disturbed/deformed
4H-1, 0–150	26.40	27.90	Soupy
4H-2, 0–138	27.90	29.28	Soupy
4H-5, 113–150	33.53	33.90	Flow-in
4H-6, 0–150	33.90	35.40	Flow-in
4H-7, 0–68	35.40	36.08	Flow-in
5H-1, 0–150	35.90	37.40	Soupy
5H-2, 0–77	37.40	38.17	Soupy
5H-3, 53–150	39.43	40.40	Flow-in
5H-4, 0–150	40.40	41.90	Flow-in
5H-5, 0–150	41.90	43.40	Flow-in
5H-6, 0–104	43.40	44.44	Flow-in
5H-7, 0–119	44.44	45.63	Flow-in
5H-CC, 0–22	45.63	45.85	Flow-in
6H-1, 0–125	45.40	46.65	Soupy
6H-2, 0–116	46.65	47.81	Soupy
6H-2, 147–150	48.12	48.15	Void
6H-6, 74–76	52.89	52.91	Void

Notes: Data from these intervals were removed from the GRA bulk density, MS, color reflectance, natural gamma, and *P*-wave velocity data sets prior to construction of the composite section. This table is also available in **ASCII**. [**N1**]

Table T5. Composite depths, Site 1222.

Core	Length (m)	Depth (mbsf)	Offset (m)	Depth (mcd)
199-1222A-				
1H	5.4	0.00	0.00	0.00
2H	9.5	5.40	–0.56	4.84
3H	9.5	14.90	1.88	16.78
4H	9.5	24.40	3.44	27.84
5H	9.5	33.90	4.88	38.78
6H	9.5	43.40	5.34	48.74
7H	9.5	52.90	9.73	62.63
8H	9.5	62.40	9.73	72.13
9X	9.6	71.90	0.00	71.90
10X	6.6	81.50	0.00	81.50
11X	9.6	88.10	0.00	88.10
12X	9.6	97.70	0.00	97.70
199-1222B-				
1H	7.4	0.00	0.00	0.00
2H	9.5	7.40	1.86	9.26
3H	9.5	16.90	2.88	19.78
4H	9.5	26.40	3.08	29.48
5H	9.5	35.90	4.80	40.70
6H	9.5	45.40	4.09	49.49
7H	9.5	54.90	4.09	58.99

Note: This table is also available in **ASCII**. [**N1**]

Table T6. Splice tie points, Site 1222.

Hole, core, section, interval (cm)	Depth (mbsf)	Depth (mcd)		Hole, core, section, interval (cm)	Depth (mbsf)	Depth (mcd)
199-				199-		
1222A-1H-3, 76	3.76	3.76	Tie to	1222B-1H-3, 76	3.76	3.76
1222B-1H-4, 116	5.66	5.66	Tie to	1222A-2H-1, 81	6.22	5.66
1222A-2H-6, 132	14.22	13.66	Tie to	1222B-2H-3, 140	11.8	13.66
1222B-2H-6, 96	15.84	17.7	Tie to	1222A-3H-1, 92	15.82	17.7
1222A-3H-5, 72	21.62	23.5	Tie to	1222B-3H-3, 72	20.62	23.5
1222B-3H-7, 16	25.56	28.44	Tie to	1222A-4H-1, 60	25	28.44
1222A-4H-7, 68	34.08	37.52	Append to	1222A-5H-1, 0	33.9	38.78
1222A-5H-7, 48	43.38	48.26	Append to	1222A-6H-1, 0	43.4	48.74
1222A-6H-7, 48	52.88	58.22	Append to	1222B-7H-1, 0	54.9	58.99
1222B-7H-6, 32	62.72	66.81	Tie to	1222A-7H-3, 118	57.08	66.81
1222A-7H-7, 48	62.38	72.11	Append to	1222A-8H-1, 0	62.4	72.13
1222A-8H-3, 114	66.54	76.27				

Note: This table is also available in **ASCII.**

Table T7. Paleomagnetic events, Site 1222.

Chron/ Subchron	Age (Ma)	Depth (mcd)
T C1n	0.000	0.00
B C1n	**0.780**	**2.72**
T C1r.1n	0.990	4.22
B C1r.1n	1.070	4.69
T C6n	19.048	42.03
B C6n	20.131	42.50
B C6Cn.3n	**24.118**	**44.56**
T C7n.1n	24.730	47.30
B C7n.1n	24.781	48.45
T C7An	25.496	49.91
B C7An	25.648	50.57
T C8n.1n	**25.823**	**51.61**
B C8n.2n	**26.554**	**55.99**
T C9n	27.027	57.46
B C9n	27.972	59.56
T C10n.1n	28.283	59.91
B C10n.2n	28.745	61.79
T C11n.1n	29.401	63.46
B C11n.2n	**30.098**	**64.90**
T C12	30.479	65.35
B C12	30.939	65.85
T C19n	41.257	75.20

Notes: T = top, B = bottom. Bold = datums used for LSR control points in Figure F10, p. 27. This table is also available in ASCII.

Table T8. Nannofossil and radiolarian events, Site 1222.

Marker species/ Zonal boundaries	Age (Ma)	Depth (mcd)	± (m)
Nannofossil events:			
NP22/23	31.70	67.85	0.12
NP10	**53.90***	**93.17**	**4.99**
Radiolarian events:			
RN12/11	2.74	19.00	0.29
RN11/10	3.87	19.38	0.19
RN10/9	4.19	22.16	0.35
RP22/21	24.60	48.23	0.75
RP21/20	29.27	63.69	0.63
RP20/19	**33.47**	**70.58**	**0.75**
RP19/18	34.77	70.58	0.75
RP18/17	36.96	72.29	0.86
RP17/16	38.12	72.29	0.86
RP16/15	**40.12**	**72.29**	**0.86**

Notes: * = midpoint age (±0.5 m.y.). Bold = datums used for LSR control in Figure **F10,** p. 27. This table is also available in **ASCII.**

Table T9. Depths, ages, rates, and fluxes of sediments, Site 1222.

Depth (mcd)	Age (Ma)	LSR (m/m.y.)	DBD (g/cm^3)	MAR (mg/cm^2/k.y.)
1.16	0.33	3.49	0.41	142
2.25	0.65	3.49	0.41	143
3.75	0.96	5.70	0.34	195
4.86	1.16	5.70	0.43	243
5.69	1.30	5.70	0.45	257
7.09	1.55	5.70	0.43	246
8.59	1.81	5.70	0.43	245
10.09	2.07	5.70	0.48	273
11.59	2.34	5.70	0.49	278
13.09	2.60	5.70	0.54	305
14.35	2.82	5.70	0.49	282
17.47	3.37	5.70	0.50	287
19.03	3.64	5.70	0.40	229
20.57	3.91	5.70	0.36	203
21.98	4.16	5.70	0.39	219
23.53	5.41	1.12	0.57	64
25.03	6.74	1.12	0.58	65
26.13	7.72	1.12	0.60	68
28.59	9.91	1.12	0.62	70
30.09	11.25	1.12	0.66	74
31.59	12.58	1.12	0.68	76
33.09	13.91	1.12	0.69	77
34.59	15.25	1.12	0.75	84
36.09	16.58	1.12	0.69	78
37.19	17.56	1.12	0.66	75
39.53	19.64	1.12	0.64	72
42.53	22.31	1.12	0.41	46
44.03	23.65	1.12	0.39	44
45.53	24.35	4.15	0.38	156
47.03	24.72	4.15	0.34	140
48.33	25.03	4.15	0.35	143
49.49	25.31	4.15	0.32	132
50.99	25.67	4.15	0.35	143
52.49	25.97	6.00	0.33	200
53.99	26.22	6.00	0.33	197
55.49	26.47	6.00	0.33	200
56.99	26.95	2.51	0.37	93
58.33	27.48	2.51	0.64	160
63.38	29.49	2.51	0.47	118
64.88	30.09	2.51	0.61	154
66.40	30.99	1.69	0.52	87
67.88	31.87	1.69	0.65	109
69.38	32.76	1.69	0.29	49
70.88	34.64	0.26	0.35	9
72.09	39.34	0.26	0.35	9
73.08	40.64	1.52	0.25	38
74.38	41.50	1.52	0.28	43
75.88	42.49	1.52	0.33	51

Notes: LSR = linear sedimentation rate, DBD = dry bulk density, MAR = mass accumulation rate. This table is also available in **ASCII**.

Table T10. Interstitial water data, Hole 1222A.

Core, section, interval (cm)	Depth (mbsf)	pH	Alkalinity (mM)	Salinity	Cl (mM)	Na (mM)	K (mM)	Ca (mM)	Mg (mM)	SO_4 (mM)	NH_4 (µM)	H_4SiO_4 (µM)	Sr (µM)	Li (µM)	Mn (µM)	Ba (µM)	B (µM)
199-1222A-																	
1H-2, 145–150	2.95	6.98	2.51	34.5	553	476	11.6	9.2	54.9	29.9	5.8	474	86	27	0.53	0.26	472
2H-3, 145–150	9.85	7.00	2.66	34.5	554	481	12.0	8.2	54.7	30.9	5.8	512	88	27	19.92	0.41	487
3H-3, 145–150	19.35	7.04	2.77	35.5	555	477	11.9	14.4	50.1	30.1	1.5	603	86	27	36.80	0.24	483
4H-3, 145–150	28.85	7.02	2.94	35.0	555	476	11.8	9.4	55.4	29.7	0.0	578	82	27	19.53	1.00	552
5H-3, 145–150	38.35	7.06	2.94	35.0	556	478	11.2	9.2	55.8	30.2	1.5	654	87	29	2.53	0.40	502
6H-3, 145–150	47.85	7.13	3.00	35.0	557	477	11.0	9.0	55.9	28.9	0.0	628	86	29	0.88	0.91	487

Note: This table is also available in **ASCII.**

Table T11. $CaCO_3$ and C_{org} data, Hole 1222A.

Core, section, interval (cm)	Depth (mbsf)	$CaCO_3$ (wt%)	Organic C (wt%)
199-1222A-			
1H-2, 74–75	2.24	0.14	
1H-4, 34–35	4.84	0.12	0.12
2H-2, 74–75	7.64	0.12	
2H-4, 73–75	10.63	0.11	0.15
2H-6, 73–74	13.63	0.14	
3H-2, 73–74	17.13	0.19	
3H-4, 73–74	20.13	0.19	0.09
3H-6, 73–74	23.13	0.18	
4H-2, 74–75	26.64	0.22	
4H-4, 74–75	29.64	1.76	0.00
4H-6, 74–75	32.64	0.14	
5H-2, 73–74	36.13	0.22	
5H-4, 73–74	39.13	0.23	0.03
5H-6, 73–74	42.13	0.28	
6H-2, 74–75	45.64	0.26	
6H-4, 74–75	48.64	0.29	0.00
6H-6, 74–75	51.64	0.29	
7H-2, 74–75	55.14	39.84	
7H-4, 73–74	58.13	67.43	0.00
7H-6, 73–74	61.13	0.57	
8H-2, 73–74	64.63	1.59	0.00

Note: This table is also available in ASCII.

Table T12. Moisture and density measurements, Hole 1222A.

Core, section, interval (cm)	Depth (mbsf)	Water content (%)	Density (g/cm^3)			Porosity (%)
			Wet bulk	Dry bulk	Grain	
199-1222A-						
1H-1, 116–118	1.16	68.0	1.27	0.41	2.63	84.5
1H-2, 75–77	2.25	68.1	1.28	0.41	2.77	85.2
1H-3, 75–77	3.75	72.3	1.24	0.34	2.69	87.3
1H-4, 36–38	4.86	66.8	1.28	0.43	2.63	83.8
2H-1, 85–87	6.25	65.2	1.30	0.45	2.60	82.6
2H-2, 75–77	7.65	66.4	1.28	0.43	2.58	83.3
2H-3, 75–77	9.15	66.3	1.27	0.43	2.46	82.5
2H-4, 75–77	10.65	63.4	1.31	0.48	2.51	80.9
2H-5, 75–77	12.15	62.7	1.31	0.49	2.44	80.0
2H-6, 75–77	13.65	60.1	1.34	0.54	2.51	78.7
2H-7, 51–53	14.91	62.6	1.32	0.49	2.56	80.7
3H-1, 69–71	15.59	62.1	1.33	0.50	2.56	80.4
3H-2, 75–77	17.15	68.3	1.27	0.40	2.58	84.4
3H-3, 79–81	18.69	71.1	1.23	0.36	2.44	85.4
3H-4, 70–72	20.10	69.0	1.24	0.39	2.38	83.8
3H-5, 75–77	21.65	57.5	1.34	0.57	2.30	75.2
3H-6, 75–77	23.15	57.0	1.34	0.58	2.29	74.8
3H-7, 35–37	24.25	55.6	1.36	0.60	2.32	74.0
4H-1, 75–77	25.15	55.4	1.39	0.62	2.48	75.1
4H-2, 75–77	26.65	53.7	1.42	0.66	2.55	74.3
4H-3, 75–77	28.15	52.5	1.43	0.68	2.52	73.1
4H-4, 75–77	29.65	52.0	1.43	0.69	2.52	72.7
4H-5, 75–77	31.15	48.6	1.46	0.75	2.45	69.3
4H-6, 75–77	32.65	51.7	1.44	0.69	2.53	72.5
4H-7, 35–37	33.75	53.1	1.42	0.66	2.51	73.5
5H-1, 75–77	34.65	54.5	1.41	0.64	2.56	75.0
5H-3, 75–77	37.65	67.8	1.26	0.41	2.44	83.4
5H-4, 75–77	39.15	68.8	1.24	0.39	2.36	83.6
5H-5, 75–77	40.65	69.3	1.23	0.38	2.23	83.1
5H-6, 75–77	42.15	72.1	1.21	0.34	2.32	85.4
5H-7, 55–57	43.45	71.6	1.22	0.35	2.30	85.0
6H-1, 75–77	44.15	73.4	1.20	0.32	2.28	86.0
6H-2, 75–77	45.65	71.7	1.22	0.35	2.39	85.6
6H-3, 75–77	47.15	72.3	1.20	0.33	2.21	84.9
6H-4, 75–77	48.65	72.9	1.21	0.33	2.40	86.3
6H-5, 75–77	50.15	72.6	1.22	0.33	2.41	86.2
6H-6, 75–77	51.65	70.1	1.23	0.37	2.36	84.3
6H-7, 59–61	52.99	54.4	1.39	0.64	2.44	74.0
7H-1, 75–77	53.65	63.8	1.31	0.47	2.52	81.3
7H-2, 75–77	55.15	56.2	1.40	0.61	2.61	76.6
7H-3, 77–79	56.67	61.4	1.34	0.52	2.68	80.6
7H-4, 75–77	58.15	54.4	1.42	0.65	2.66	75.6
7H-5, 75–77	59.65	75.8	1.20	0.29	2.50	88.4
7H-6, 75–77	61.15	71.9	1.23	0.35	2.59	86.6
7H-7, 46–48	62.36	71.8	1.23	0.35	2.48	86.0
8H-1, 95–97	63.35	78.9	1.18	0.25	2.63	90.6
8H-2, 75–77	64.65	76.1	1.19	0.28	2.45	88.4
8H-3, 75–77	66.15	72.7	1.22	0.33	2.50	86.6

Note: This table is also available in ASCII.

Table T13. LAS-based mineralogy, Hole 1222A.

Core, section, interval (cm)	Depth (mbsf)	Calcite (model wt%)	Opal (model wt%)	Smectite (model wt%)	Illite (model wt%)
199-1222A-					
1H-1, 24–26	0.25	24.5	21.1	0.0	54.4
1H-1, 82–84	0.83	14.0	13.8	0.0	72.2
1H-1, 116–118	1.17	14.2	4.2	9.8	71.8
1H-1, 125–127	1.26	16.4	1.3	9.5	72.8
1H-2, 24–26	1.75	13.5	0.3	22.1	64.1
1H-2, 75–77	2.26	17.9	3.0	24.7	54.5
1H-2, 125–127	2.76	21.4	0.0	18.9	59.7
1H-3, 24–26	3.25	8.6	6.6	30.1	54.6
1H-3, 75–77	3.76	7.7	10.5	48.4	33.4
1H-3, 125–127	4.26	4.2	14.3	36.2	45.3
1H-4, 24–26	4.75	11.9	5.7	50.8	31.7
1H-4, 36–38	4.87	18.6	2.3	40.2	39.0
1H-4, 60–62	5.11	11.2	7.3	42.4	39.1
2H-1, 85–87	6.26	12.0	5.9	51.2	30.8
2H-1, 124–126	6.65	26.6	0.0	19.9	53.4
2H-2, 23–25	7.14	33.1	0.0	27.2	39.7
2H-2, 75–77	7.66	12.3	0.0	66.0	21.7
2H-3, 23–25	8.64	0.0	22.9	74.3	2.9
2H-3, 75–77	9.16	0.0	20.1	78.0	2.0
2H-4, 23–25	10.14	0.0	26.6	73.4	0.0
2H-4, 75–77	10.66	0.0	25.5	60.1	14.5
2H-5, 23–25	11.64	8.4	16.0	66.9	8.7
2H-5, 75–77	12.16	0.0	28.2	71.8	0.0
2H-6, 23–25	13.14	13.8	5.3	80.9	0.0
2H-6, 75–77	13.66	17.3	0.0	82.7	0.0
2H-7, 23–25	14.64	5.7	6.3	88.0	0.0
2H-7, 51–53	14.92	24.8	0.0	64.5	10.7
3H-1, 69–71	15.60	26.2	0.0	67.1	6.8
3H-1, 123–125	16.14	46.3	0.0	17.1	36.5
3H-2, 23–25	16.64	48.2	0.0	0.0	51.8
3H-2, 75–77	17.16	30.3	24.8	31.3	13.7
3H-3, 23–25	18.14	50.2	0.5	6.5	42.9
3H-3, 79–81	18.70	31.6	31.3	30.0	7.1
3H-4, 23–25	19.64	44.1	12.4	8.4	35.2
3H-4, 70–72	20.11	46.2	38.2	0.0	15.5
3H-5, 23–25	21.14	9.3	4.9	85.8	0.0
3H-5, 75–77	21.66	12.5	0.0	87.5	0.0
3H-6, 23–25	22.64	11.8	0.0	88.2	0.0
3H-6, 75–77	23.16	11.7	0.0	88.3	0.0
3H-7, 23–25	24.14	20.9	0.0	79.1	0.0
3H-7, 35–37	24.26	14.1	0.0	85.9	0.0
4H-1, 23–25	24.64	24.0	0.0	76.0	0.0
4H-1, 75–77	25.16	29.8	0.0	66.4	3.8
4H-1, 124–126	25.65	28.8	0.0	65.9	5.2
4H-2, 23–25	26.14	34.6	0.0	60.1	5.3
4H-2, 75–77	26.66	25.2	0.0	61.1	13.7
4H-3, 23–25	27.64	27.6	0.0	62.5	9.9
4H-3, 75–77	28.16	24.6	0.0	68.4	7.1
4H-4, 23–25	29.14	28.1	0.0	51.8	20.1
4H-4, 75–77	29.66	22.3	0.0	60.1	17.5
4H-5, 23–25	30.64	35.4	0.0	39.3	25.4
4H-5, 75–77	31.16	29.3	0.0	51.1	19.7
4H-6, 23–25	32.14	43.0	0.0	8.3	48.7
4H-6, 75–77	32.66	34.6	0.0	43.8	21.6
4H-7, 23–25	33.64	36.6	0.0	36.1	27.3
4H-7, 35–37	33.76	35.2	0.0	45.1	19.7
5H-1, 75–77	34.66	43.4	0.0	30.8	25.8
5H-1, 123–125	35.14	45.3	0.0	29.2	25.5
5H-2, 23–25	35.64	45.7	0.0	24.9	29.4
5H-2, 75–77	36.16	43.9	0.0	43.4	12.7
5H-3, 23–25	37.14	30.9	0.0	59.1	10.0
5H-3, 75–77	37.66	0.0	0.0	100.0	0.0
5H-4, 23–25	38.64	0.0	4.0	96.0	0.0
5H-4, 75–77	39.16	1.5	0.0	98.5	0.0
5H-5, 23–25	40.14	0.0	0.0	100.0	0.0
5H-5, 75–77	40.66	0.0	0.2	99.8	0.0
5H-6, 23–25	41.64	42.4	4.0	32.2	21.4
5H-6, 75–77	42.16	32.6	17.2	39.3	10.8
5H-7, 23–25	43.14	44.8	8.8	21.4	25.0
5H-7, 55–57	43.46	30.9	15.0	40.3	13.7
6H-1, 75–77	44.16	32.2	19.9	33.7	14.3
6H-1, 123–125	44.64	39.1	19.0	18.3	23.6
6H-2, 23–25	45.14	36.8	19.1	23.8	20.3
6H-2, 75–77	45.66	31.0	14.1	39.6	15.3
6H-3, 23–25	46.64	37.5	14.7	22.0	25.8
6H-3, 75–77	47.16	25.3	27.0	39.7	8.0
6H-4, 23–25	48.14	39.9	17.0	17.1	25.9
6H-4, 75–77	48.66	32.4	14.9	37.0	15.7
6H-5, 23–25	49.64	38.3	11.0	28.9	21.8
6H-5, 75–77	50.16	33.3	14.2	40.7	11.9
6H-6, 23–25	51.14	42.5	11.5	24.7	21.3
6H-6, 75–77	51.66	31.6	15.9	41.5	10.9
6H-7, 23–25	52.64	57.9	0.0	41.1	0.9
6H-7, 59–61	53.00	41.3	4.1	54.6	0.0
7H-1, 75–77	53.66	30.0	0.0	70.0	0.0
7H-2, 75–77	55.16	54.5	0.0	45.5	0.0
7H-3, 77–79	56.68	60.1	3.1	36.7	0.0
7H-4, 75–77	58.15	79.6	3.9	9.2	7.4
7H-5, 75–77	59.66	51.1	24.5	24.0	0.4
7H-6, 75–77	61.16	0.0	0.0	100.0	0.0
7H-7, 46–48	62.37	0.0	0.0	100.0	0.0
8H-1, 95–97	63.36	0.0	0.0	100.0	0.0
8H-1, 123–125	63.64	7.9	0.0	92.1	0.0
8H-2, 23–25	64.14	0.0	0.0	100.0	0.0
8H-2, 75–77	64.66	0.0	0.0	100.0	0.0
8H-3, 23–25	65.64	0.0	1.7	98.3	0.0
8H-3, 75–77	66.16	0.0	0.0	100.0	0.0

Note: This table is also available in ASCII. [N1]

Table T14. Split-core velocity measurements, Hole 1222A.

Core, section, interval (cm)	Depth (mbsf)	Velocity (m/s)			Anisotropy (%)
		z*	y*	x†	
199-1222A-					
1H-1, 117	1.17	1486	1511		1.7
1H-2, 76	2.26	1482	1497		1.0
1H-3, 76	3.76	1486	1502		1.1
1H-4, 37	4.87	1483	1496		0.9
2H-1, 86	6.26	1481	1497		1.1
2H-2, 76	7.66	1481	1493		0.8
2H-3, 76	8.89			1530	
2H-4, 76	10.66	1483	1493		0.7
2H-5, 76	12.16	1485	1496		0.8
2H-6, 76	13.66	1492	1501		0.6
2H-7, 52	14.92	1487	1502		1.0
3H-1, 70	15.60	1488	1516		1.9
3H-2, 76	17.16	1494	1512		1.2
3H-3, 80	18.70	1498	1518		1.3
3H-4, 71	20.11			1558	
3H-5, 76	21.66	1491	1502		0.7
3H-6, 76	23.16	1490	1502		0.8
3H-7, 36	24.26	1492	1512		1.3
4H-1, 76	25.16	1496	1510		1.0
4H-2, 76	26.66	1502	1516		0.9
4H-3, 76	28.16	1499	1514		1.0
4H-4, 76	29.66	1496	1525		2.0
4H-5, 76	31.16	1500	1513		0.8
4H-6, 76	32.66	1503	1515		0.8
4H-7, 36	33.76	1501	1520		1.3
5H-1, 76	34.66	1504	1532		1.9
5H-2, 76	36.16	1507		1531	1.5
5H-3, 76	37.66	1498	1521		1.5
5H-4, 76	39.16			1517	
5H-5, 76	40.66			1512	
5H-6, 76	42.16			1528	
5H-7, 56	43.46			1542	
6H-1, 76	44.16			1558	
6H-2, 76	45.66			1563	
6H-3, 76	47.16			1554	
6H-4, 76	48.66			1540	
6H-5, 76	50.16			1556	
6H-6, 76	51.66			1562	
6H-7, 60	53.00			1533	
7H-1, 76	53.66			1524	
7H-2, 76	55.16			1522	
7H-3, 78	56.68			1520	
7H-4, 76	58.16			1515	
7H-5, 76	59.66			1543	
7H-6, 76	61.16			1534	
7H-7, 47	62.37			1528	
8H-1, 95	63.35			1515	
8H-2, 76	64.66			1518	
8H-3, 76	66.16			1519	

Notes: * = determined by insertion probe, † = determined by contact probe. This table is also available in ASCII.

Table T15. Thermal conductivity, Site 1222.

Core, section, interval (cm)	Depth (mbsf)	Thermal conductivity (W/[m·K])
199-1222A-		
1H-3, 76	3.76	0.74
2H-3, 76	9.16	0.75
3H-3, 76	18.66	0.73
4H-3, 76	28.16	0.82
5H-3, 76	37.66	0.76
6H-3, 76	47.16	0.73
7H-3, 76	56.66	0.82
8H-3, 76	66.16	0.71
199-1222B-		
1H-3, 76	3.76	0.73
2H-3, 76	11.16	0.80
3H-3, 76	20.66	0.80
4H-3, 76	30.16	0.81
6H-3, 72	48.87	0.69
7H-3, 76	58.66	0.75

Note: This table is also available in **ASCII.**

CHAPTER NOTE

N1. 13 December 2002—After the CD-ROM version of this volume was published, errors were noted in the ASCII versions of Tables T4, T5, and T13. This version contains the corrected ASCII files.

---

*Dates reflect file corrections or revisions.